Bulletin of Volcanology (2024) 86:22
https://doi.org/10.1007/s00445-024-01719-7

RESEARCH ARTICLE

Feedback responses between endogenous and exogenous processes at Campi Flegrei caldera dynamics, Italy

Sambit Sahoo[1] · Bhaskar Kundu[1] · Simona Petrosino[2] · Rajeev K. Yadav[3] · Deepak K. Tiwari[1] · Shuanggen Jin[4,5]

Received: 22 July 2023 / Accepted: 15 February 2024

Abstract

The Campi Flegrei caldera is characterized by the phenomenon of bradyseism, as evidenced by stratigraphic records of alternate oceanic and continental sediments dating back over a thousand years. Since 2005, the caldera has been in a phase of unrest, which is increasing volcanic deformations and associated seismicity around the region, resulting in a growing concern over the dense population in the inhabitation. Recent studies have highlighted that the caldera dynamics are driven by a combination of endogenous processes and modulation phenomena induced by exogenous processes, e.g., rainfall, atmospheric pressure, and tidal loading. Although the complex feedback mechanisms of both endogenous and exogenous processes are still under debate, the present study is focused on the increased potential of modulation due to exogenous processes with the increase or evolution in the degree of inflation of the magma chamber. Specifically, Campi Flegrei volcanic system shows sensitivity to seasonal hydrological cycles during slower rates of inflation and to short-period tidal modulations during higher rates of inflation. The observed seasonal modulations of seismic activity are explained in terms of water infiltration into the shallow aquifers, basins, and vent depression system of the caldera. The rainfall-induced pore pressure build-up also favours the instability of the brittle cap rock, promoting seismicity. In addition, this study suggests that the tidal loadings provide horizontal NS extensions to the mostly NW–SE, NE–SW, and EW-oriented scattered fractures and further contribute towards fracture propagation. During this process, a cyclic opening and sealing of fractures by volatile outgassing and silicate settling may, respectively, produce the episodic behaviour of the seismicity. The seismicity in relation to exogenous processes imposed by seasonal rainfall and tidal loadings shows that the degree of correlation depends on the different rates of inflation. The long-period seasonal modulations and short-period tidal modulations during the evolution of the degree of inflation are finally interpreted in the framework of the fault resonance destabilization model, under rate-and-state dependant frictional formalism.

Keywords Bradyseism · Inflation · Endogenous and exogenous process · Fault resonance · Caldera

Abbreviations

CF	Campi Flegrei
Mc	Magnitude completeness
SRI	Slower rate of inflation
HRI	Higher rate of inflation
RSF	Rate and state friction

Introduction

Volcanoes are complex systems on which the dynamics are often determined by the interplay between endogenous and exogenous processes (Wilcock et al., 2016; Petrosino et al. 2018; Tan et al. 2018; Sahoo et al. 2021; Dumont et al. 2022a). Several studies have shown that in active volcanic or hydrothermal systems, the exogenous process

Editorial responsibility: N. Fournier

✉ Bhaskar Kundu
rilbhaskar@gmail.com

[1] Department of Earth and Atmospheric Sciences, NIT Rourkela, Rourkela 769008, India

[2] Instituto Nazionale Di Geofisica E Vulcanologia, Sezione Di Napoli - Osservatorio Vesuviano, 80124 Naples, Italy

[3] CSIR-National Geophysical Research Institute, Hyderabad, Telangana 500007, India

[4] School of Surveying and Land Information Engineering, Henan Polytechnic University, Jiaozuo 454000, China

[5] Shanghai Astronomical Observatory, Chinese Academy of Sciences, Shanghai 200030, China

Published online: 01 March 2024

can modulate volcanic activity, and the degree of modulation is maximum during metastable states and unrest. The exogenous sources which can cause stress perturbations include various processes such as rainfall-induced seasonal fluid pore pressure changes (Hainzl et al. 2006; Farquharson and Amelung 2020), seasonal atmospheric pressure and thermal cycles contributing to variation of the lithostatic pressure and ground temperature (Petrosino et al. 2018; Chiodini et al. 2015), and tidal loading (Hamilton 1973; Mcnutt and Beavan 1987; Rydelek et al. 1988; Emter 1997; Sahoo et al. 2021, 2022; Niu and Song 2021) acting on short and long time scales, which possibly trigger brittle deformations and eruptions (Dumont et al. 2022a). Seasonal rainfall modulations are reported from various active volcanoes and even non-volcanic tremors (Hainzl et al. 2006; Mason et al. 2004; Pollitz et al. 2013). Similarly, tidally triggered non-volcanic tremors are reported in many parts of the world (Cochran et al. 2004; Métivier et al. 2009. Theoretically, short-period stress perturbations as tidal modulations can occur in a system with high loading velocity and constant periodic tidal loading (Lockner and Beeler 1999; Perfettini et al. 2001; Senapati et al. 2022, 2023). The tidal modulations are observed when the pore fluid pressure equals the lithostatic pressure, which can only be achieved during the critical state of pre-eruption (Thomas et al. 2012). So, it can be suggested that the volcanic systems will provide a higher degree of correlation of exogenous processes with the endogenous manifestations (e.g., seismicity) associated with a high degree of inflation and/or under a critical state (Wilcock et al., 2016; Petrosino et al. 2018; Sahoo et al. 2021).

The Campi Flegrei (CF) caldera, in southern Italy, is a typical example of such volcanic systems. Here, the hydrological cycles strongly influence its activity in terms of earthquakes and ground deformation (Petrosino et al. 2018, 2021a; Scafetta and Mazzarella 2021). Moreover, the CF caldera, located in a coastal region, experiences moderate ocean tidal loading, which provides a substantial degree of exogenous effects on the internal dynamics (De Lauro et al. 2013; Petrosino et al. 2018; Falanga et al. 2019; Petrosino and Dumont 2022). The history of settlements in the CF region dates back to the Palaeolithic age as the volcanic eruptions have made the land fertile and abundant with hot springs and lakes, making it an ideal place for inhabitation. At present, the region is home to more than 350,000 people, posing serious questions about volcanic risk management (Kilburn et al. 2017; Orsi et al. 2004). For preparedness for volcanic hazards and risk mitigation in the CF region, intense studies have been performed (Orsi et al. 2004; Mastrolorenzo et al. 2006; Kilburn et al. 2017; Carlino 2021), which were also used by the Italian government for planning a possible evacuation of the population. Therefore, the *i* estimation of the probability of an eruption as well as the assessment of the volcanic hazard is of much priority for this densely populated region.

The present study focuses on the correlation of the ground deformation, associated seismicity modulations, and their relation between endogenous and exogenous processes during the accelerated rate of inflation at CF caldera. In order to estimate the degree of correlation between endogenous and exogenous processes, we have used different physical parameters and observations (e.g., ground deformation, seismicity, rainfall, air temperature and pressure, ground temperature, and ground tilt). Based on the ground deformation and seismicity rates, we have differentiated the timespan of observation (1 January 2005–31 December 2019) in two intervals: Slower Rate of Inflation, SRI, (2005–2013) and Higher Rate of Inflation, HRI, (2014–2019). We have used the GNSS time series to model the location and geometry of the deformation source and degree of inflation using the inversion approach. The effect of tidal loading on the volcanic system and associated tidal modulations have been analysed using correlation techniques and tidal stress modelling, respectively. We have also investigated the possibility of resonance destabilization process during the two different phases of inflation and the associated degree of correlation with long-period and short-period stress perturbations. On the basis of the results, we propose a possible model which relates the mechanism of the ground deformation and the seasonal and tidal modulations of the seismicity. Our studies can be useful to better understand the degree of inflation at CF caldera and the possible evolution of the dynamics of the volcanic system, contributing to the volcanic hazard and risk assessment during emergency mitigation.

Campi Flegrei caldera: geological setting, ground deformation, magmatic system, and hydrothermal circulation

The CF caldera is a complex volcanic system covering around 450 km^2 to the west of the city of Naples, with a long history of deformation and eruption episodes (Orsi et al. 1996; Di Vito et al. 1999). The region is cut by high-angle faults or fractures with NW–SE and NE–SW trends in a radiating pattern that extends from latitude 40.75° to 40.9° N and longitude 14° to 14.25° E. The CF caldera is a nested structure with a diameter of more than 10 km which was formed due to subsequent collapses dated back 39,000 years ago (Campanian Ignimbrite) and 15,000 years ago (Neapolitan Yellow Tuff) (Fig. 1). Since then, more than ~ 70 smaller eruptions have formed several craters and vents inside the large CF caldera complex, both on land and submerged under the Pozzuoli Bay (Orsi et al. 1996; Vito et al. 1999). The eruption of CF has been magmatic to phreatomagmatic,

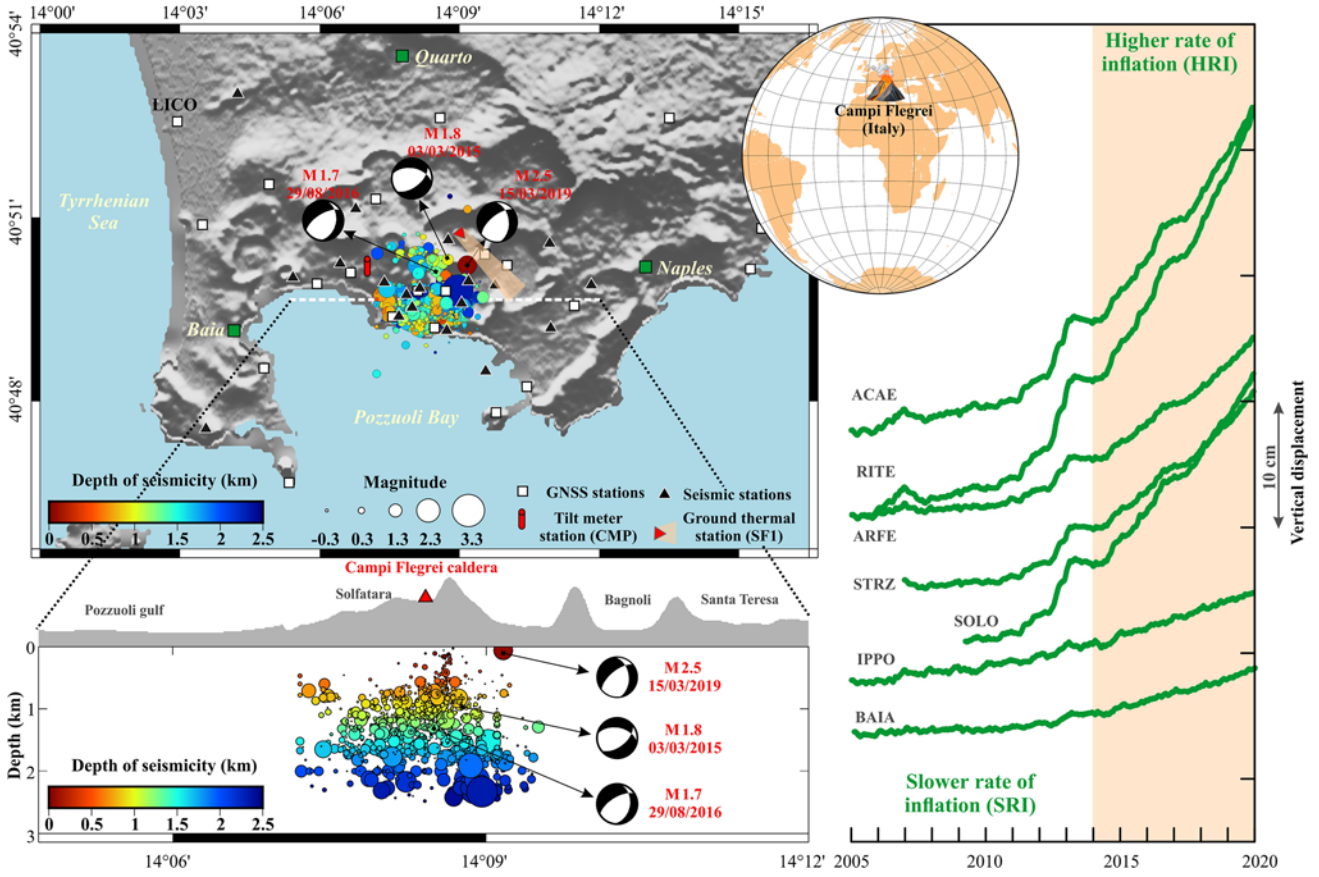

Fig. 1 General morphology, seismicity and GNSS observations at the Campi Flegrei caldera, Italy. The globe inset shows the region of Campi Flegrei Caldera. **Top** White rectangles are the GNSS stations. Black triangles mark the location of Seismic stations. Seismicity is shown in colour size scale as represented along with fault plane solution of random events. **Bottom** Seismicity with respect to depth along with fault plane solution of random events is shown at the respective cross-section (white dashed line at the **Top**). **Right** The vertical displacements observed in the region at different GNSS stations

with tephra fallouts and pyroclastic currents causing significant damage to the settlements (Di Vito et al. 1999; Orsi et al. 2004). Stratigraphic evidence shows widespread volcanic ash deposits around the region, which provides an idea about the effective radius of the volcanic eruption (Orsi et al. 1996; Di Vito et al. 1999). The last eruption occurred in 1538, giving rise to the new dome at Monte Nuovo (Di Vito et al. 1987, 1999).

The history of the CF caldera is associated with periodic ground movements of uplift and subsidence known as bradyseism (i.e., slow ground movement in Greek) (Parascandola 1947). Documentation regarding the ground movements dates back to the eighth century, corresponding to the stratigraphy of the region with alternative marine and continental sediments. The historic ground movement is evident in the marble columns at the Macellum of Serapeo (ancient marketplace of Romans), where the molluscan tracks and trails are observed at ~ 7 m in height (Parascandola 1947). After the Monte Nuovo eruption, the CF caldera underwent a phase of subsidence, interrupted by major and minor ground uplifts, the most recent of which occurred in 1950, 1969–1972, 1982–1984, 1989, 1994, and 2000 (Del Gaudio et al. 2010). The uplift phases are characterized by the occurrence of volcano-tectonic earthquakes that significantly increase during the unrest phases. On the contrary, during the subsidence, seismicity is scarce (Bellucci Sessa et al. 2021). The earthquakes often occur in swarms and are generated by brittle shear failure mechanisms caused by the pressurization of the hydrothermal system and fluid flow towards the surface (Saccorotti et al. 2007; De Lauro et al. 2016). Most seismic events are located at shallow depths (4 km below sea level), beneath the Solfatara-Pozzuoli area (Bellucci Sessa et al. 2021; Petrosino et al. 2018).

Since 2005, the CF caldera has undergone an almost continuous uplift but with variable rates: (a) a lower rate up to 2014, interrupted by two short-time acceleration episodes in 2006 and 2012 (De Martino et al. 2014) and (b) a continuous accelerating trend starting from 2014 (Fig. 1). The overall vertical deformation is about 115 cm to date (Campi

Felgrei Caldera, Monthly Surveillance Bulletin, September 2023 available at the URL www.ov.ingv.it).

The prominent vertical ground movements during particular events in the history of bradyseism provide information related to the repeated magma injections and progressive structure formation in and around the CF caldera system (Chiodini et al. 2012). Since 1950, the ground displacements are maximum around the town of Pozzuoli and reduced towards the margin of a spherical boundary with centres beneath Pozzuoli, i.e., the Solfatara crater, suggesting the presence of a constant spheroidal magma source (Lima et al. 2021). The Solfatara crater is a constant source of fumarolic emissions, mainly from Bocca Grande, Bocca Nova, and Pisciarelli, containing mainly CO_2/H_2O which are due to the interaction of magmatic-hydrothermal fluids into the surface hydrothermal system and meteoric water (Chiodini et al. 2012).

The magma source and injection of magmatic fluids have been a subject of discussion, and different hypotheses have been suggested as the source location and mode of fluid transport (Tedesco 1994; De Natale et al. 2001). The seismic tomography has provided evidence of a shallow gas reservoir (2–3 km) with low Vp/Vs values beneath the CF caldera (Battaglia et al. 2008; De Siena et al. 2010). According to Calò and Tramelli (2018), high Vp/Vs and low Vp/Vs values at different depths suggest the presence of different anomalous bodies. The shallow-depth aquifers and volatile-rich rock layers are represented by the low Vp/Vs layers which extended a maximum of up to 2 km. The high Vp/Vs values are related to the hydrothermal fluid conduits at a depth of 2–4 km and the magmatic source below. The scattering values suggest the presence of low scattering water-filled fractured rocks in the first km of depth and deeper (1–2 km) high scattering volatile-rich fractured rocks, i.e., the most likely source of the observed seismicity. The gravity inversion study by Capuano et al. (2013) shows similar results. The deeper part of the magmatic complex is separated from the shallow aquifer by impermeable layers mainly composed of volcanoclastic sediments and marine deposits (de Vivo et al. 1989; Calò and Tramelli 2018). Below the hydrothermal reservoir, the contact aureoles represent the depths of magma injection, and the change in grades of metamorphism contributes to the change in permeability of the corresponding rocks (Vivo et al. 1989). At ~ 7 km depth, a layer of igneous sill detected by the seismic tomography (Zollo et al. 2008) has been interpreted as a magma intrusion and source of the steam-rich magmatic fluids that fed the shallow reservoir (Moretti et al. 2018). The permeability of the layers plays an important role in controlling the ground displacement, as the strata provide quasi-barriers to the upward movement of magmatic fluid and gases as well as the downward movement of meteoric water (Lima et al. 2009). The displacement due to inflation may be of different degrees according to the location of the hydrothermal pressure, being higher at the shallow impermeable layer and lower at the bottom magma injection layer. Also, the duration of the uplift phase depends on the duration of hydrothermal recharge and obstruction from the impermeable layer (Lima et al. 2009). The magmatic injections generate an increase of CO_2 fluids in the volcanic system and a consequent increment of CO_2/H_2O ratio in the surface gas emissions during the inflation phases (Chiodini et al. 2010, 2012). The fluid migration also causes the formation of fractures and their propagation in the low permeability cap rock, thus promoting seismicity (Lima et al. 2021; Petrosino and De Siena 2021). Observations of diverse geophysical and geochemical parameters suggest various phases of inflation and deflation during the historical period, and that currently, the volcanic system is at a higher degree of inflation (Troise et al. 2019; De Martino et al. 2021).

Datasets and methodology

GNSS displacements

The ground displacements are monitored by the Neopolitan Volcanoes Continuous GNSS (NeVoCGPS) network from the GNSS stations located around the CF. The network is maintained by Istituto Nazionale di Geofisica e Vulcanologia–Osservatorio Vesuviano (INGV-OV), and it is composed of 21 stations, with some stations having continuous operations since 2000 (De Martino et al. 2021). The stations provide high accuracy of vertical and horizontal displacements which is collected and analysed for inflation and deflation-related information. Datasets of 2005–2019 are publicly archived from De Martino et al., (2021) (Figure S1).

Seismicity catalogue

The seismicity catalogue of the CF earthquakes is compiled by the INGV-OV observatory, publicly available on the domain http://sismolab.ov.ingv.it/sismo/index.php?PAGE=SISMO/last&area=Flegrei. The INGV-OV makes joint use of a permanent and a mobile network composed of velocimeters and accelerometers for the seismological monitoring of the CF region (https://www.ov.ingv.it/index.php/monitoraggio-sismologico/flegrei-monit-sism). The seismic stations are both analogue and digital, with installations at terrestrial and marine platforms. In the present work, we have used the re-located volcano-tectonic events which occurred at CF caldera from 2005 to 2019. The seismicity catalogue contains 1343 well-located events with magnitudes ranging from – 1.0 to 3.1, hypocentral depths of up to 3 km below sea level, and a variety of earthquake focal mechanisms, with primarily normal faulting due to CF

caldera collapse structures (Fig. 1). The seismicity rate has gradually increased with a maximum rate at the end of the investigated timespan (Bellucci Sessa et al. 2021). The highest magnitude of 3.1 occurred in December 2019. As a preliminary step, we performed a statistical analysis of the seismic catalogue, by estimating the completeness magnitude, *b*-value, and periodicity (Supplementary Text) (Figure S2, S3). From the catalogue, we have observed an increase in the number of events with respect to time due to the volcanic unrest. As the detection threshold of a seismic network can be characterized by the completeness magnitude Mc which is almost constant (−0.3) for the whole time interval, we can reasonably be confident that the increase in the earthquake rate is not due to the increase in the number of seismic stations. For the statistical analysis described in the next sections, we used relocated earthquakes above the estimated threshold of Mc = −0.3. In addition, we worked on both non-declustered (raw) and declustered catalogues because the two have different statistical properties (Petrosino et al. 2018). In fact, at CF caldera, there are many seismic swarms that could bias the results of some methodologies (such as the Schuster spectrum; see "Tidal periodicity of seismicity and correlation with tidal loading" section). At the same time, seismic swarms are a relevant component in the CF seismicity, so it is important to consider them when one applies different techniques (such as correlation analyses; see "Relationship between seismicity and rainfall" section).

Meteorological and hydrological data

The hydrological changes during the year at CF caldera consist of wet and dry seasons which go from September to March and from April to August, respectively. The rainfall amount is measured by local weather stations and archived in public repositories. As the study interval is very long (2005–2019), data from two different public archives (i.e., https://www.wunderground.com/weather/it/positano/LIRN/date/20194, https://www.3bmeteo.com/meteo/ora/storico/202201) were combined to generate the total dataset with daily observations for the whole investigated timespan. We have also considered satellite-derived rainfall observations from GPM (ftp://arthurhou.pps.eosdis.nasa.gov/gpmdata). Atmospheric observations such as pressure and temperature were obtained from the public archive https://www.wunderground.com/weather/it/positano/LIRN/date/20194n. The land surface displacement/deformation due to the change in rainfall causing seasonal hydrological mass variation has been estimated at GNSS site coordinates by using the data archived from the German Research Center for Geosciences (GFZ) (http://rz-vm115.gfz-potsdam.de:8080/repository).

The Hydrological Land Surface Discharge Model (LSDM), version v1.3, precisely computes the elastic deformation in the centre of the Earth's frame. It includes the satellite-estimated mass of soil moisture, snow, and surface water in rivers and lakes on a 24-h basis on a regular grid of 0.5° × 0.5° (Dill and Dobslaw 2013). This closely follows the deformations on seasonal and shorter timescales (Dong and Kelly 2003) based on the modelled load Love numbers considered for an elastic Earth model "ak135" (Wang et al. 2012). For predicting hydrologically induced displacements at a station, the LSDM model uses numerical model simulations, which explain a considerable fraction (up to 54% on a global scale) of the naturally observed vertical movements at the station caused by seasonal hydrological loading variations (Dill and Dobslaw 2013).

Ground temperature and tilt data

The thermal infrared camera network (Vilardo et al. 2008; Caputo et al. 2020; Cusano et al. 2021a; Sansivero and Vilardo 2022) and the borehole tiltmeter networks (Ricco et al. 2019; Petrosino et al. 2021a, b) provide continuous datasets for ground temperature and ground tilt measurements, respectively. The networks are managed by INGV-OV. Although only recent observations are available from these instruments (Cusano et al. 2021a, 2021b; Petrosino et al. 2021a, 2021b), the specific datasets which cover part of the whole time span of 2005–2019 have been analysed for supportive correlations. Specifically, we have used the ground temperature data from the SF1 infrared thermal camera (Cusano et al. 2021b) and the root mean square (RMS) of ground tilt data from the CMP tiltmeter (Petrosino et al. 2021b) (Figure S3).

Solid earth and ocean tidal loading models

For quantification of tidal loading, the longitudinal strains (north 0° and east 90°), shear strains (north-east), and volumetric strain (vertical) acting on the major fault azimuth at a central point over the CF Caldera (40.83° N, 14.14° E) have been estimated due to combined ocean tides and body tidal loading using the SPOTL program (Agnew 1996, 1997, 2012). This program assumes an elastic and spherical earth (degree-two Love numbers $h = 0.6114$, $k = 0.3040$, and $l = 0.0832$) using Cartwright–Tayler constituent amplitudes and Green's functions from the Gutenberg–Bullen earth model (Farrell 1972) and computes the tidal strains directly from the positions of the moon and the sun (Agnew 1997). The strains (extension positive) were obtained for the eight major short-period tidal constituents (K1, K2, M2, N2, O1, P1, Q1, and S2) using the GOT4.7, a global ocean tidal model (Richard Ray 1999) combined with the Oregon State University (OSU) regional ocean tidal model for the Mediterranean and the Black Seas (Egbert and Erofeeva 2002). In the present computation, we considered an Elastic modulus of 5 GPa and a Poisson ratio of 0.25 (Manconi et al. 2010;

Sahoo et al. 2021). We computed the horizontal north–south (NS), horizontal east–west (EW), and volumetric/vertical stresses on the CF caldera by converting strains to stress, adopting linear elastic constitutive equations.

Results

Observation and modelling of the deformation source

Changes in the uplift rate related to CF caldera are clearly visible in the vertical displacements recorded by GNSS stations from 2005 to 2019 (Fig. 1). In fact, until 2013, the deformations show multiple episodes of small uplifts (e.g., 2006 and 2012) (De Martino et al. 2014) with a time span greater than 0.23 years and a velocity greater than 18 mm/year, whereas since 2014, the deformation rate accelerates almost continuously (Fig. 1). Also, from the temporal analysis of Mc and *b*-value, we have found that their fluctuations significantly increase after 2014 (Supplementary Text; Figure S2) which is also coherent with the changes in inflation. This motivated further for the temporal segmentation; considering both instances of the observed changes, we have differentiated the whole time interval (2005–2019) into two timespans of active inflation, namely Slower Rate of Inflation, SRI (2005–2013) and Higher Rate of Inflation, HRI (2014–2019).

We have attempted to model the CF source of deformation in order to assess the inflation rates in the two timespans. We used the dMODELS software package (Battaglia et al. 2013), with the source of deformation assumed to be spherical with a radius of 500 m and located in a flat, homogeneous, elastic, and isotropic half-space (as for the shallow gas-saturated hydrothermal reservoir inferred by Calò & Tramelli 2018). We have performed GNSS inversion (Battaglia et al. 2013), which analyses the average displacement rates measured by the GNSS stations around the deformation source, to determine the rate of inflation and location of the source (modelling methods described in the Supplementary Text). The average displacements observed at the GNSS stations are used as input alongside the standard Lamé's constants, and the priori vent location is set at the Solfatara crater, based on the outcomes of recent studies (e.g.Amoruso and Crescentini 2022 and references therein). The change in volume of the reservoir is defined as the following equation (Table S1) (McTigue 1987; Battaglia et al. 2013):

$$\Delta V = \pi a^3 \frac{\Delta P}{\mu}\left[1 + \left(\frac{a}{z_0}\right)^4\right] \quad (1)$$

where ΔP is the pressure change and the ratio of the source radius, and depth ($\frac{a}{z_0}$) is the expansion (e). We have also used different models (i.e., spherical, spheroidal, and sill) and obtained the respective results as well as the goodness-of-fit by chi-square statistical test (Supplementary Text; Table S1, Figure S5-S8). We found that the spherical model has better statistics compared to other models in the form of chi-square values (i.e., closer to 1) and other parameters. For the spherical model, a least-square inversion scheme was performed on the observed deformation at various GPS stations to get the best-fit solution for the vent location, which lies within a search radius of 5000 m. The dimensionless pressure change, source depth, and volume change from 250 solutions were generated randomly for a limited range of these model parameters.

The inferred rates (slower and higher) from the GNSS displacement observations with standard values of elastic constants as Lamé's constant and shear modulus were taken into account for the modelled estimations (Kiyoo 1958; McTigue 1987). From visual inspections, we can suggest that the estimations of horizontal and vertical displacements were well-fitted with the observed values in the case of the HRI due to constant uplift (Fig. 2). Also, from the statistical results with higher chi-square value (i.e., closer to 1) and lower standard deviations from the average/mean displacement modelled values, we can suggest that the model has a better fit during the HRI (Figure S9-S12). Overall, the SRI had minor mismatches as the timespan contains multiple uplift episodes of variable rates (i.e., 2006 and 2012).

The source of the inflation was estimated beneath the Solfatara crater (Fig. 2), at a depth of around 3.7 km and 2.8 km (in SRI and HRI, respectively), which is compatible with the presence of the hydrothermal reservoir where the probable mixing between hydrothermal and magmatic fluids occurs. This provides the constraints regarding the processes involved in the inflation mechanisms. The source modelling confirmed the variation in uplift rates causing the differences in vertical displacements (Figure S10-S13). According to the previous assumptions in different studies, we have adopted a Poisson ratio (ϑ) = 0.25 and shear modulus (μ) = 5 GPa for the modelling (Amoruso et al., 2008; Trasatti et al. 2015; Manconi et al. 2010; Heap et al., 2014) (Supplementary Text). The dimensionless pressure change ($\Delta P/\mu$) was found to be 1.63×10^{-3} and 5.11×10^{-3} during the SRI and HRI, respectively. This also provided the volume increase of the reservoir ΔV from $6.3\,9 \times 10^5$ m^3 year^{-1} during the SRI to 2.01×10^6 m^3 year^{-1} during the HRI (Table S2).

Exogenous processes on CF caldera

We have performed a power spectrum analysis on daily and hourly bins of both observed and synthetic time series of various datasets to identify the periodicities (Fig. 3) (method described in Supplementary Text). This provides information on the effective perturbation periods of the exogenous

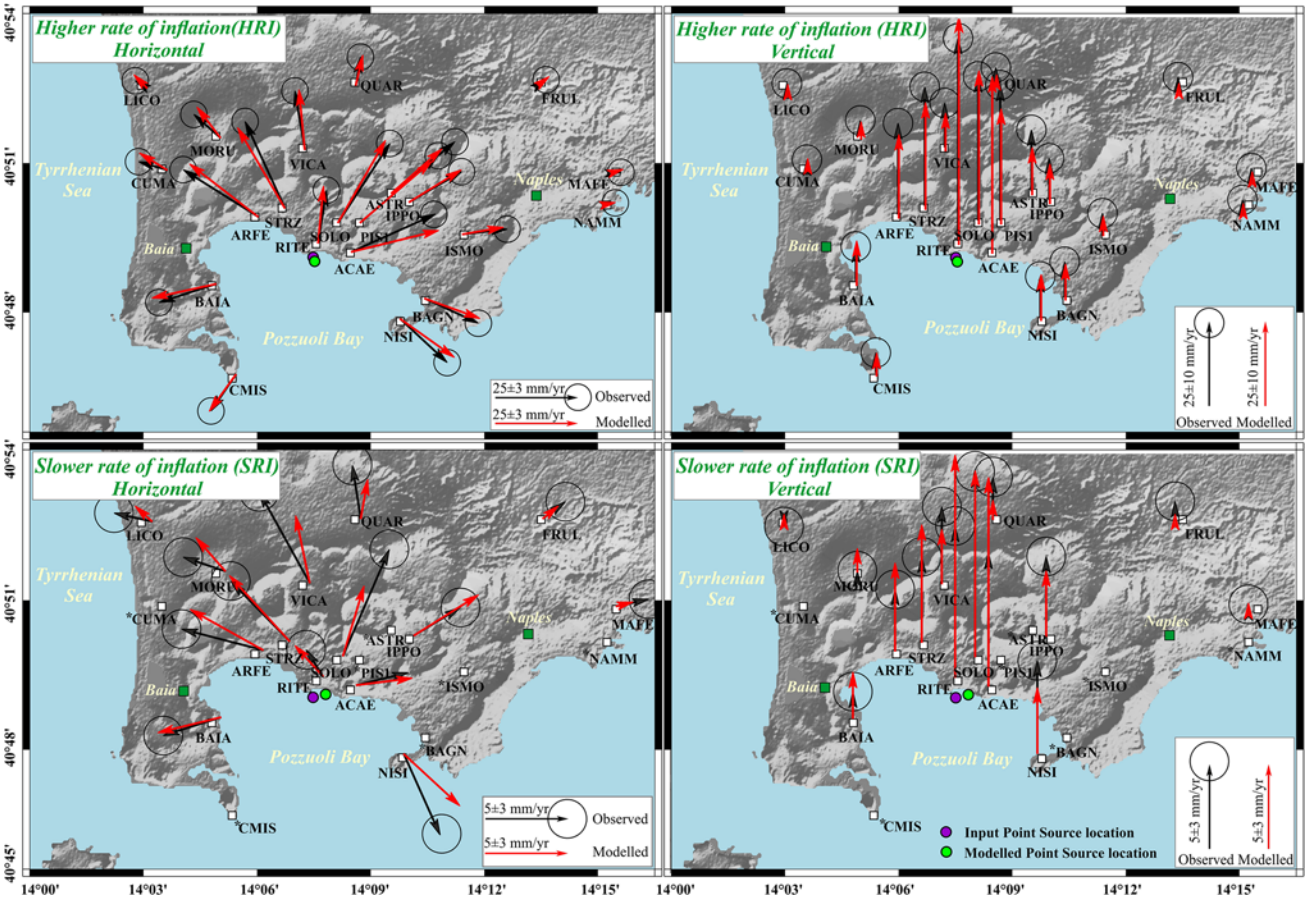

Fig. 2 Comparison of the average horizontal and vertical displacements during different timespans of SRI (2005–2013) and HRI (2014–2019) which are observed from the GNSS stations (black arrows) and modelled from the inversion using dMODELS (red arrows). The black circles represent the error units of the observed GNSS stations. The violet circle represents the input point source and the green circle represents the model-estimated point source location

process acting on the CF caldera and the effects generated on it. We observe that pressure, temperature, and rainfall observations all exhibit substantial annual periodicity, suggesting that these variables act as an exogenous process on ground tilt and LSDM displacements (Fig. 3). Possibly because of the greater amount of precipitation during the wet season, rainfall exhibits a semi-annual periodicity, but this does not appear to affect the other physical observations with the exception of the declustered seismicity, which also displays a weak semi-annual peak. Diurnal and semi-diurnal periodicities in the seismicity, as well as modelled tidal stress data, are revealed by power spectrum analysis of hourly bins. We further investigated the correlation between the seasonal time-scale of the seismicity with the observables exhibiting annual periodicity (rainfall, tilt, atmospheric pressure, and LSDM displacements) by calculating their average cumulated monthly distributions (Fig. 4). The results demonstrate a strong relationship between seismicity and the seasonal trends of the other observables, indicating that exogenous processes like precipitation, atmospheric pressure, and temperature positively affect the CF seismicity on seasonal time scales. Based on these findings, we investigated how annual as well as short-period tidal stress perturbations from various sources might affect the seismic activity in the CF caldera in the subsequent sections.

Relationship between seismicity and rainfall

The region of CF caldera experiences a temperate climate of the northern hemisphere with alternate wet (September–March) and dry seasons (April–August), with November being the month getting maximum rainfall. On average, the wet season receives rainfall of ~ 120 mm per month, and the dry season ~ 40 mm per month (Petrosino et al. 2018). A large amount of rainfall in the wet seasons induces variations of the pore-fluid pressure at depth to affect the hydrothermal circulation beneath the surface of the CF caldera (Scafetta and Mazzarella 2021; Petrosino et al. 2021a). To estimate the effect, we have computed the pore-fluid pressure changes at different depths in response to surface rainfall.

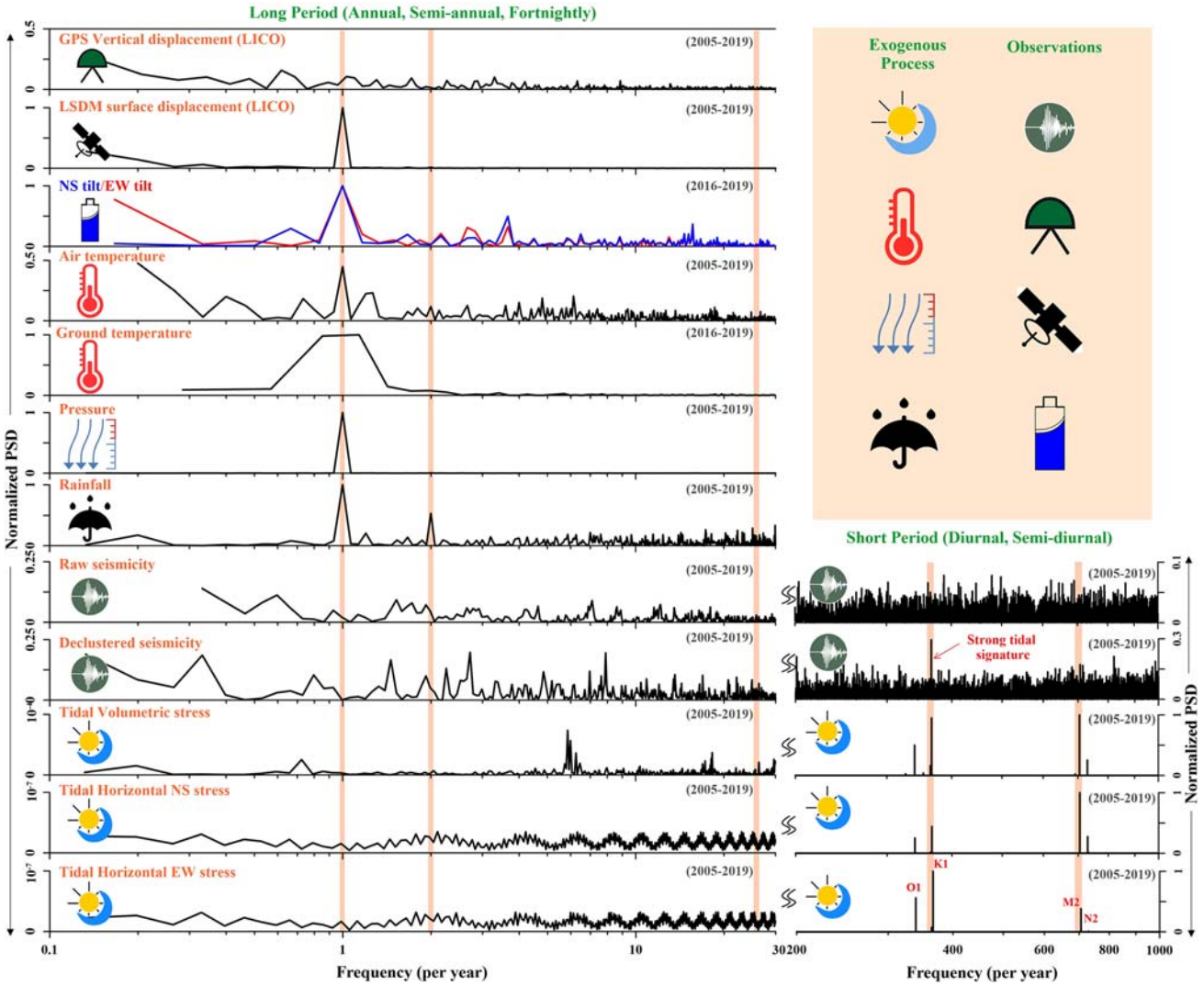

Fig. 3 Power spectra of the exogenous processes (both observed and modelled) (tidal loadings, air and ground temperatures, atmospheric pressure, and rainfall) acting on the caldera and observational data (seismicity, vertical and horizontal displacement, LSDM surface displacement, and ground tilt). O1 and K1 indicate the diurnal tidal constituents; M2 and N2 indicate the semi-diurnal tidal constituents

The transient and vertical groundwater flow is solved using a finite-difference approximation method. Subsurface pore-pressure perturbations have been computed as a function of diffusion of rainwater into the surface, which under mathematical approximations can be represented as (Rudnicki 1986; Barton and Barton 1989):

$$\frac{\delta p}{\delta t} = \left[\frac{kK}{\mu\varphi}\right]\left[\frac{\delta 2p}{\delta h2}\right] \tag{2}$$

where pore pressure exerted by the rainwater is represented by p, over a time period of t, at a depth of h below the ground surface, and a function of hydraulic diffusivity $\left[\frac{kK}{\mu\varphi}\right]$ (i.e., a function of the permeability of the host k, bulk modulus K, percolating fluid (rainwater) viscosity μ, and porosity of the host rock φ). To avoid boundary effects in the depth-range of our interest, a zero-flux boundary is imposed at the base depth of the domain h, which is considered 10 km beneath the surface in this case. We acknowledge that the tectonic and hydro-magmatic framework of the CF caldera is complex; however, with the lack of accurate estimates of hydrological parameters beneath the CF caldera, we have assumed representative hydrogeological model parameters with four different models (Models I to IV) (Farquharson and Amelung 2020) (Supplementary Text).

It is observed that the temporal distribution of raw (not declustered) seismicity during both the SRI and HRI well matches the pore pressure changes associated with rainfall (Fig. 5). It can be perceived that the seismicity rate increases with a higher amount of rainfall, contributing

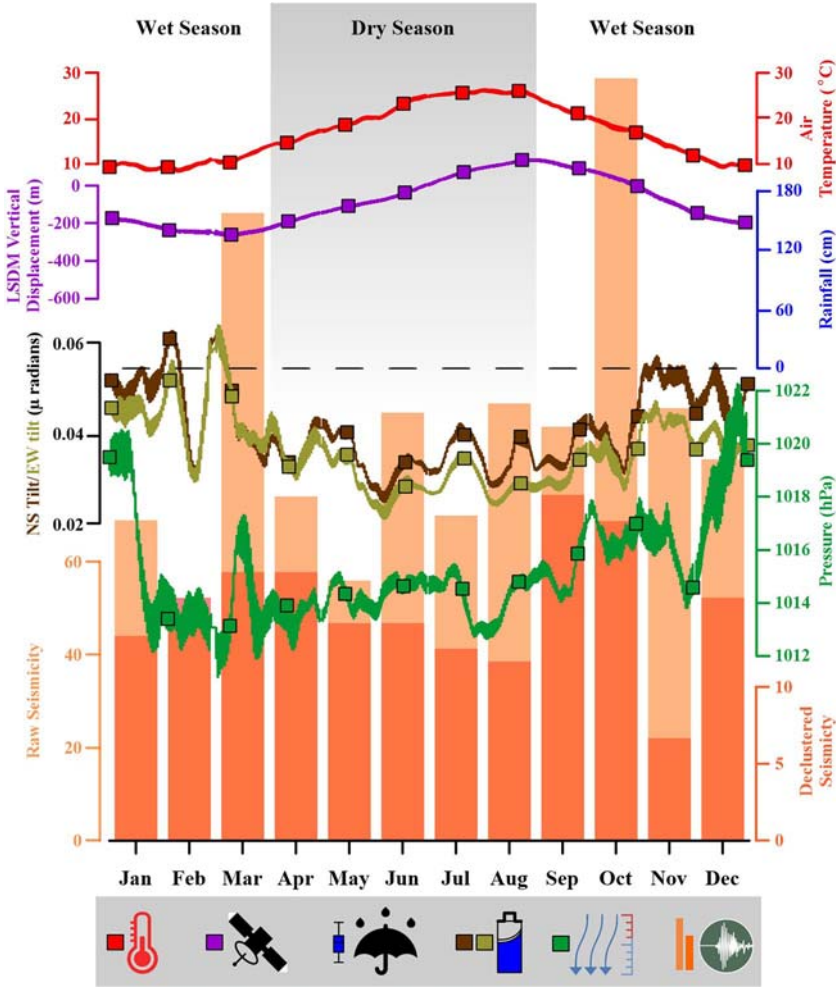

Fig. 4 Average cumulated monthly histogram of seismicity (raw and declustered) showing correlation with average cumulated monthly graphs of atmospheric pressure, ground tilt, rainfall (ground observations), LSDM vertical displacement, and air temperature

to increasing the pore pressure at the corresponding depth of the earthquake foci. Further, we have performed a lag-correlation analysis on the monthly cumulative seismicity and rainfall during the two different inflation phases (Fig. 6). The seismicity and rainfall appear closely correlated, except for the declustered seismicity in the HRI. During the SRI and HRI, we observe a semi-annual pattern of rainfall and seismicity as well. For further statistical robustness, we have also performed a lag-correlation analysis on the seismicity, rainfall, and associated pore pressure (Fig. 6). During the SRI, seismicity (both raw and declustered), rainfall, and pore pressure are well correlated with each other. During the HRI, the raw seismicity still has a good correlation with rainfall, whereas the declustered seismicity is not well correlated (Fig. 6). These observations provide evidence of an interaction of meteoric water with the hydrothermal reservoir, but its effect is either absent or being suppressed in case of the declustered seismicity during the HRI, likely due to the presence of additional external stress from other contributors.

Tidal periodicity of seismicity and correlation with tidal loading

As the short-period tidal periodicities (diurnal and semi-diurnal) were observed in the power spectra analysis of seismicity (Fig. 3), we have done a detailed periodicity analysis for the two different inflation timespans (Fig. 7). The Schuster spectrum (Ader and Avouac 2013) and power spectra analysis are performed on the declustered catalogue, and it can be observed that there is an absence (at 99% confidence level of the Schuster test) of short-period components in the seismicity observed during the SRI, whereas during the HRI, a strong semi-diurnal (M2) periodicity is observed (Fig. 7). This suggests the presence of tidal loading effects on the seismicity occurrence during the HRI.

It has been reported that the effect of tidal loading on the respective source of deformation depends on various factors like fault orientations and pore fluid pressures. (Cochran et al. 2004; Tanaka et al. 2006; Métivier et al. 2009). In order to gain more insight into these relationships, we performed

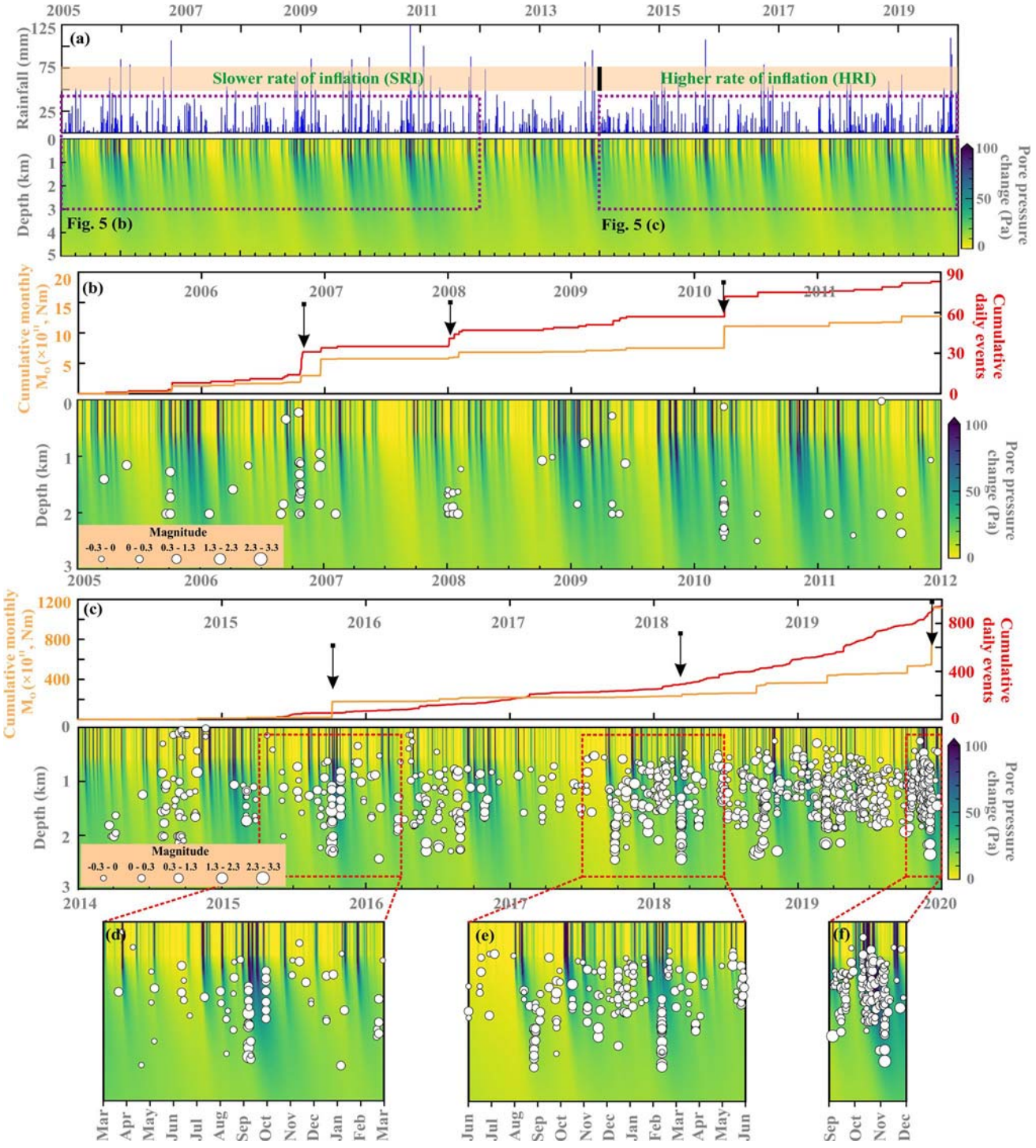

Fig. 5 **a** Time series correlation between average rainfall (GPM), calculated pore pressure change using Model-II (see suppl. Figure S16), and raw seismicity during the SRI and HRI. **b** and **c** are the insets of representative time intervals from the SRI and HRI. **d**, **e**, and **f** are zoomed insets of representative time intervals from the HRI

a tidal correlation analysis of seismicity with tidal loading. The region of CF has a diverse orientation of fault planes; hence, we have considered the overall horizontal (NS and EW) and vertical/volumetric stress acting on the CF caldera. The representative tidal time series (Fig. 8a) is estimated, considering the contribution from total tidal loading (ocean + solid earth). Further, the phase of the occurrence of each earthquake with corresponding tidal stress variation has been estimated by

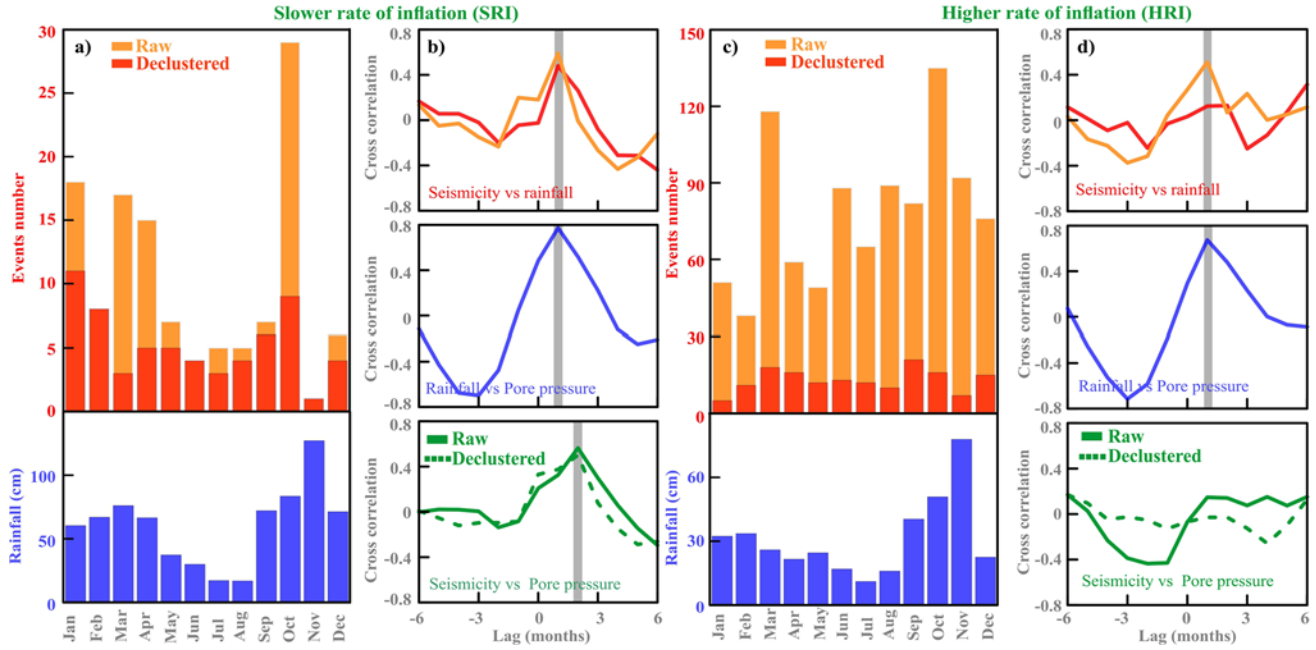

Fig. 6 Histogram showing the correlation between seismicity (raw and declustered) and rainfall during the SRI (**a**) and HRI (**c**). Lag correlation of seismicity (raw and declustered) with rainfall and pore pressure, as well as the correlation of rainfall with pore pressure during the SRI (**b**) and HRI (**d**)

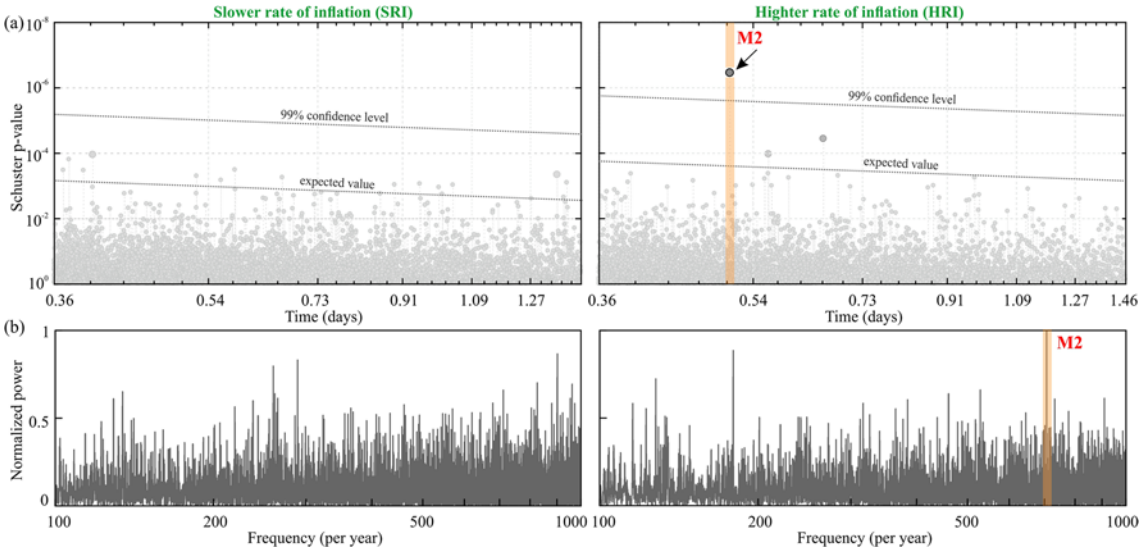

Fig. 7 Periodicity analysis using the Schuster spectrum (**a**) and power spectrum (**b**) of declustered seismicity during the SRI and HRI. Note that the seismicity during the HRI has a semi-diurnal periodicity corresponding to the M2 semidiurnal tidal constituent

defining the phase of each occurrence in the respective tidal time series between 0 and 360°. The 0 and 360° represent the two alternate peaks of the tidal stress (Fig. 8b). To analyse the degree of correlation between seismicity and tidal loading, we have performed the excess event analysis by computing the percentage of the number of excess events (N_{ex}) (Cochran et al. 2004; Thomas et al. 2012; Sahoo et al. 2021), which are the difference between the observed and expected number of events divided by the expected number of events as follows:

$$\text{Percentage of excess event } (N_{ex}) = \frac{N_{observed} - N_{expected}}{N_{expected}} \times 100 \quad (3)$$

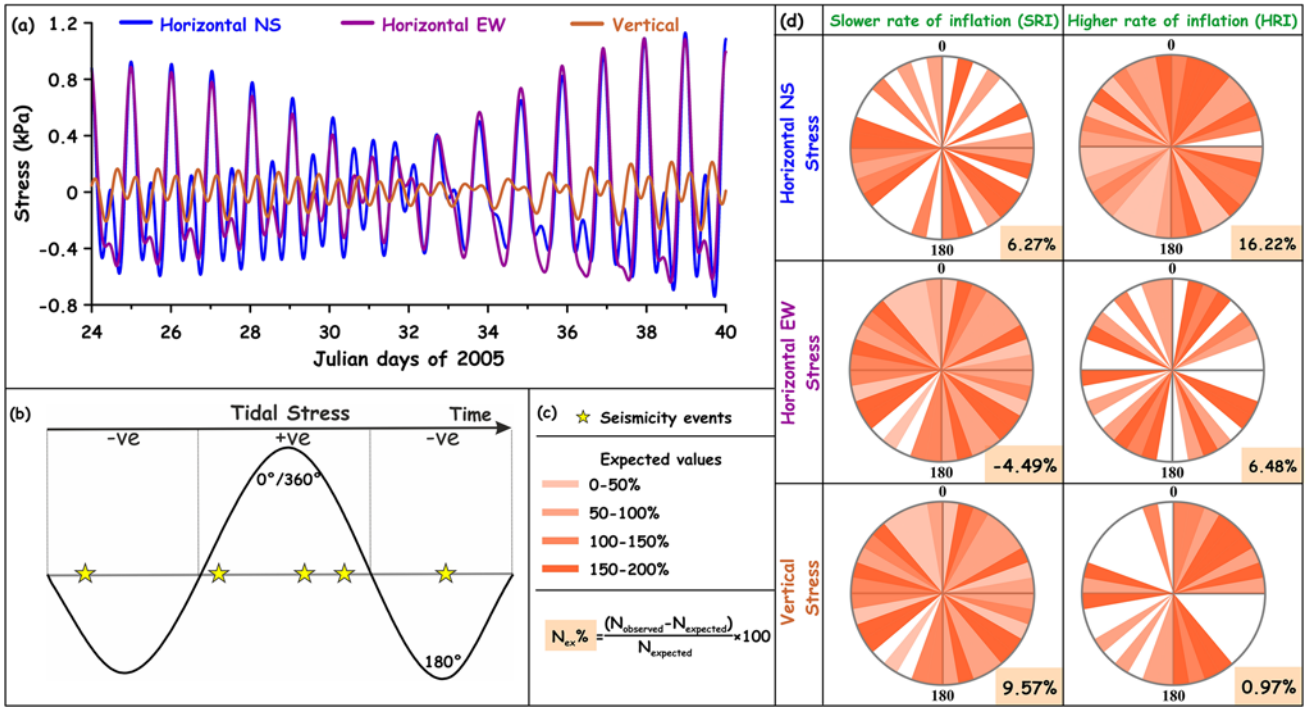

Fig. 8 **a** Representative tidal stress time series at the Campi Flegrei caldera. **b** A schematic diagram of tidal stress time series with positive and negative domains are shown, respectively. Yellow stars represent hypothetical earthquakes. **c** The schematic phase plots are denoted with different colours for the 50%, 100%, 150%, and 200% expected value bins which represent the $N_{ex}+1$ ratio percentage of the events. **d** Phase plot of declustered catalogue (Mc = −0.3) for the different phases of inflation (i.e., SRI (left) and HRI (right), respectively). The N_{ex} percentage for each plot is shown at the bottom of each plot

$N_{expected}$ is the number of expected events, i.e., the number of events under positive tidal stress conditions, assuming the random distribution of events at times. $N_{observed}$ is the observed number of events during positive stress conditions. Positive N_{ex} values suggest an excess of events, and negative N_{ex} values suggest a deficiency of events under positive tidal stress conditions (Cochran et al. 2004; Thomas et al. 2012; Sahoo et al. 2021). The results are represented using a polar bar chart for the declustered seismicity catalogues during the SRI and HRI by combining the phases of all the seismic events in 10° bins. Each bin is normalized by the expected number of events in the respective range based on the distribution of tidal stress (Fig. 8d). Therefore, the concerned colour scale of the polar bar chart represents the ratio of the observed and expected number of events ($N_{ex}+1$) for the particular range of phase (Fig. 8d). Also, the expected value has been represented as the different colour patterns for different percentage values (50, 100, 150, and 200) (Fig. 8c). When the ratio of the events or the radius of the bin in the polar bar chart is more than 100% expected value, it suggests a strong correlation between tidal stress with the events. We observe that the seismicity that occurred during the HRI has a more significant correlation with the horizontal NS tidal stress (Fig. 8d). The positive N_{ex} values and the ratio of observed to expected events above 100% expected value colour pattern suggest that the excess number of events occur during extensional horizontal NS stress. From this, we can infer that during extension, the pore spaces were dilated, thus facilitating the movement of hydrothermal fluids and generating brittle deformations due to the pressure increase. This enhanced the gas emission at the Solfatara crater during the HRI compared to the SRI, consistent with the experimental observations by Chiodini et al. (2021).

Fault resonance process on magma chamber inflation

Although periodic tidal loading and seasonal rainfall-induced stress perturbation are at the order of Pa to kPa range, the domain remains sensitive to resonance destabilization and seismicity modulation under rate-and-state friction (RSF) (Perfettini et al. 2001; Senapati et al. 2022, 2023). To probe the exact frictional condition and sensitivity of the triggering potential of the seismicity at the CF caldera, a long-period and short-period exogenous process-induced resonance destabilization model was developed (modelling approach described in Supplementary Text). We have tested the possibility of resonance amplification assuming RSF and looked for the model parameters that could justify resonance amplification and

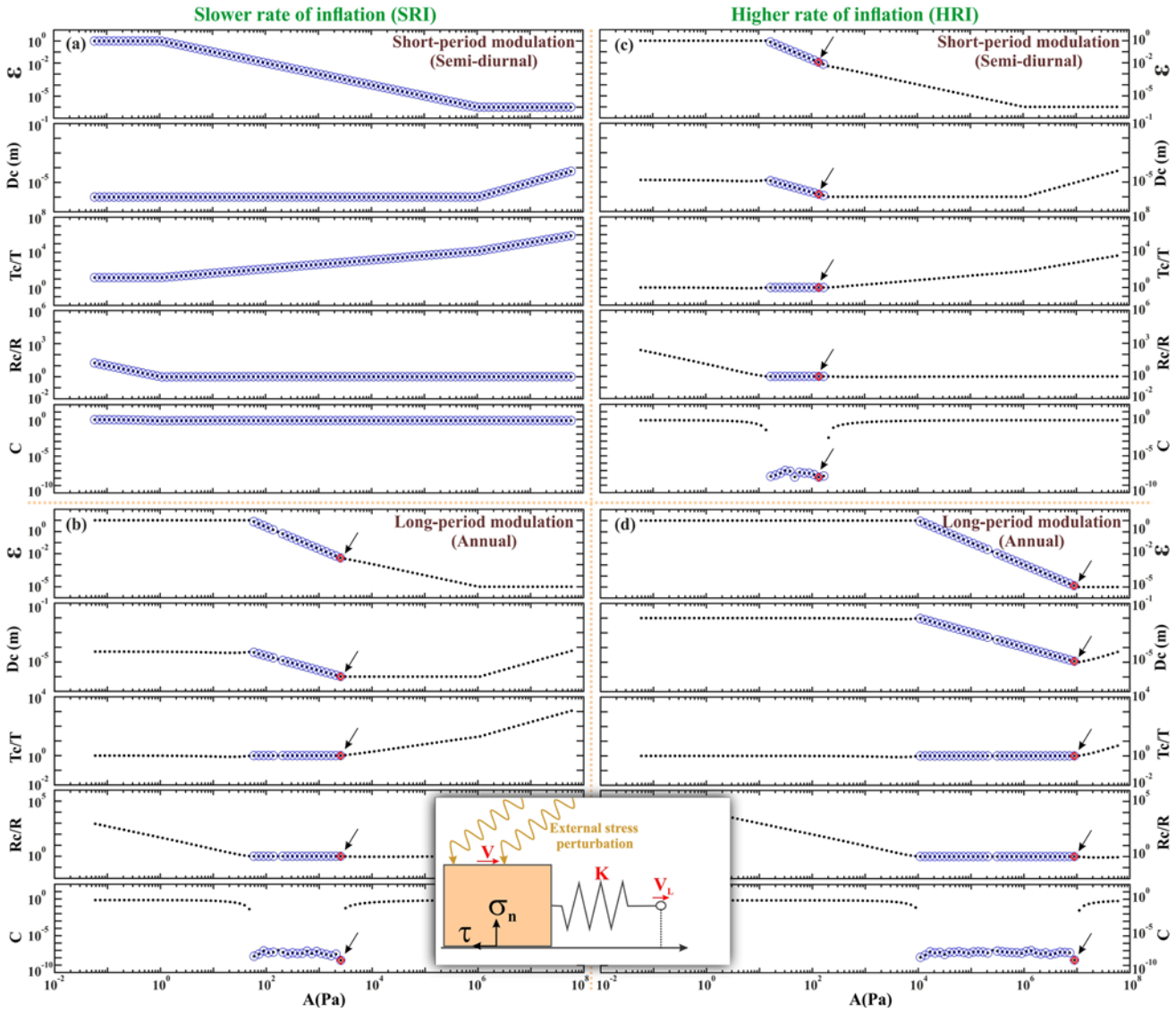

Fig. 9 Variations of the best-fit parameters of ε, dc, T/Tc, Rc/T, and C as a function of the A parameter for the present case. The best-fit model value corresponds to the red square, and the blue circles define the range of acceptable model values (Tables S3 and S4). We considered forcing a semi-diurnal period for the short-period modulation and an annual period for the long-period modulation (characteristic size $R = 4$ km; depth, $z = 2$ km), considering the variable degree of magma chamber inflation during the SRI and HRI, respectively (SRI ~ 5 mm/year and HRI ~ 25 mm/year). Inset shows a model of exogenous processes on a block moving on a plane with rate (V), inflation rate (V_L), and resistance (K) with the block providing normal stress (σ_n) and shear stress (τ) on the plane

seismicity modulation at the CF (Fig. 9). To characterize the resonance destabilization mechanism related to exogenous seasonal rainfall and tidal-induced stress perturbations, three criteria need to be satisfied. The period of excitation (T) must be close to the critical period of excitation (T_c), the length of the fault patch (R) must be close to the critical length of the fault patch (R_c), and finally, the cost function (C) should be very close to zero along with the critical slip distance (d_c). The value of frictional parameters "a" and "b" are determined from the laboratory experiments which define the stability of the fault zone by the corresponding "$b - a$" value (Scholz, 1998). Also, the rational parameter ε can defy the stability of the zone as it is the ratio of $b - a$ to a. Figure 9 represents the derived values ε, d_c, T/T_c, R/R_c, and C as a function of controlling parameter A (product of frictional constant parameter a and effective normal stress σ_*). For this computation, we assume specific periods of resonance modulation as long-period annual (seasonal stress perturbation), short-period semi-diurnal (tidal stress perturbation $M2$) (time period T as annual = 1 year and semi-diurnal $M2 = 12.42$ h), and depth z as 2 km considering the variable degree of magma

chamber inflation during the SRI and HRI, respectively (SRI ~ 5 mm/year and HRI ~ 25 mm/year).

The best-fit model parameter corresponds to the red circle symbol, and the blue circles represent the range of admissible models for which the cost function is reasonably small (Fig. 9). All the panels in Fig. 9, except the short-period tidal stress perturbations during the SRI, show only a limited range of A yields to low values of the cost function C. From this, it appears that for the resonance model to apply to the rest cases, d_c should have a narrow range of variations from 10^{-6} to 10^{-5} m (Fig. 9, Table S3, S4). The estimated value of d_c is consistent with the laboratory value of d_c from the rock friction experiments (Marone 1998). As $\frac{b}{a} = 1 + \varepsilon$, which indicates that $\frac{b}{a}$ is close to 1. In the RSF framework, the region is expected to exist at the zone of destabilization during the HRI for both seasonal and tidal stress perturbations, whereas during the SRI, the destabilization zone exists only for seasonal perturbations.

Moreover, the parameter $A = a\sigma*$ varies in the range of $10^3 - 10^4$ Pa (Fig. 9, Table S3, S4). From that, we have calculated the effective normal stress as $\sigma_* = \frac{A}{a}$, assuming $a = 10^{-4} - 10^{-2}$ as in laboratory experiments (Marone 1998). It has been observed that the effective normal stress is very low compared to the lithostatic stress (Tables S3, S4), indicating the presence of high pore pressure at the CF caldera during cases of resonance destabilization. Therefore, we can infer that during the HRI, both seasonal (long-period) and tidal (short-period) perturbations can be responsible for resonance destabilization and seismicity modulation. Still, during the SRI, only the seasonal (long-period) perturbations provide the resonance destabilization process for seismicity modulation.

Discussions

Inflation variations at the CF caldera

Globally, it has been noted that the majority of volcanic unrests are followed by eruptions (Newhall CG & Dzurisin D (1988); Phillipson et al. 2013); however, the unrest events are not multiple and episodic without eruptions, as in the exceptional case of the CF caldera. Here, major and small episodes of uplift and subsidence occurred during the CF caldera history without any eruption. The horizontal displacements are crucial for depicting the source of the inflation (Bevilacqua et al. 2015). For the considered study timespan (i.e., 2005–2019), on a long time scale, the inflation rate varies significantly in the pre- and post-2014 intervals (i.e., SRI and HRI). In addition, small and short-time episodes of uplift can be observed too (i.e., 2006 and 2012) (Fig. 1). The observed and modelled displacements that we obtained during the HRI show that the source of deformation is beneath Solfatara crater (i.e., the location of the spherical source in the finite modelling) (Fig. 2). The estimated displacements from the model well-fit the observed ones during the HRI (Figure S10). On the other hand, the estimated displacements have minor mismatches with the observed values during the SRI (Figure S9). Such dissimilarity in the observed and the estimated values may be due to the occurrence of the small uplift episodes of 2006 and 2012 (De Martino et al. 2014; Lima et al. 2021). In fact, the superposition of different components associated with the source dynamics can produce a deviation of the deformation pattern from the background trend (Falanga et al. 2023).

Several studies on the source of the surface deformation were carried out by analysing displacement observations from InSAR and GNSS, using different techniques. Such studies aimed at the source modelling (Amoruso et al. 2014a, Amoruso et al. 2014b, Amoruso and Crescentini 2022), providing constraints on the mechanisms of ground deformation (Manconi et al. 2010; D'Auria et al. 2011; Trasatti et al. 2015) and on the possible location of vent opening (Bevilacqua et al. 2020). D'Auria et al. 2011, D'Auria et al. 2015) suggested the presence of magma emplacements at depths around 3–4 km represented by igneous sill-like structures which are formed due to short or medium eruptions resulting from the magma injections at different times (Trasatti et al. 2015). Further, the expansion of volatile gases and/or expansion of the magmatic emplacements can be the causes of deformations, as recently suggested by Nespoli et al. (2021) who explained the inflation by the expansion of the gas-filled thermo-poro-elastic (TPE) inclusions or fractured reservoir rocks in nature.

Taking into account these extensive studies and the results of our modelling, we infer that the observed ground deformation at CF caldera is sourced by the expansion of a relatively small volume located at a depth between 2.8 and 3.7 km within the Solfatara hydrothermal system. The pressurization of this reservoir is likely induced by magmatic fluid injections from the deeper magma body located below, or by an increased degassing rate of the reservoir due to the mixing of hydrothermal fluids. The depth variation during the different time intervals (SRI and HRI) could be due to the change in the rate of inflation of the finite point source, as an increase/decrease in inflation during the HRI/SRI provides the depth estimates in a lesser/greater range. So in fact, the interaction of a finite body with the surface is generally in the form of expansions (e) which is a power of the radius (a) to depth (z) ratio ($e = a/z$). As we have used constant radius values for the two intervals (SRI and HRI), the variation of the source depth can be an artefact due to the actual change in the source radius due to inflation (Supplementary Text, Figure S12, S13). The observed variation is within the accepted range of the chi-square estimation values derived from the correlation between depth and pressure change

(Supplementary Text, Figure S9). In any case, the difference of about 1 km of depth between the SRI and HRI would not affect the proposed interpretation of inflation of the shallow reservoir. Despite its limits, the model is sensitive enough to quantify the volumetric changes of the deformation source in the SRI and HRI, providing useful constraints on the inflation processes.

Response of the hydrothermal system to exogenous processes

From the periodicity analysis of the physical observations, we observed that the atmospheric pressure, temperature, and rainfall exert maximum seasonal stress, and the tidal stress perturbations exert maximum semi-diurnal and diurnal stress on the CF caldera system (Fig. 3). Indeed, the volcanic and hydrothermal systems are sensitive to exogenous sources (Hainzl et al. 2006; Farquharson and Amelung 2020; Chiodini et al. 2015; Hamilton 1973; Mcnutt and Beavan 1987; Rydelek et al. 1988; Sahoo et al. 2022), especially when they are in a nearly critical state (Petrosino et al. 2018; Sahoo et al. 2021; Petrosino and Dumont 2022; Dumont et al. 2022a).

CF caldera has experienced multiple major unrests characterized by rapid inflations (Lima et al. 2021), which are accompanied by an increase in the CO_2/H_2O ratio and seismicity (Chiodini et al. 2012, 2021). This testifies to the importance of fluid movement and magmatic gas emissions in the inflation/deflation phases of the CF volcanic system. The seismicity occurs at shallow depths (2–3 km), above the deeper (> 6–7 km) magmatic emplacements promoting brittle deformations in the surficial rocks. The mechanism of such brittle deformation has been explained by invoking gas movements in the shallow reservoir and emissions associated with thermodynamics and crystallization as well as fluid exsolution (Lima et al. 2009; Chiodini et al. 2017, 2021). The responsible processes for such seismicity modulations can be related to the exogenous processes as previously explained. So, the seasonal recurrence and short-period tidal periodicities that we observe in the seismicity suggest that the exogenous processes such as rainfall and associated pore pressure changes, atmospheric pressure and temperature, and tidal loading affect the fluid circulation at the shallow hydrothermal reservoir of the CF volcanic system. This also affects the dynamics of fracture propagation and the generation of additional deformations that increase gas emission as well as seismicity.

Rainfall-induced modulation and associated pore pressure change

The mechanisms of hydro-mechanical coupling between rainfall and ground include the load from the added water mass or the diffusion-related pore pressure change and induced instability of the low-permeability cap rock (Kümpel et al. 2001; Lesparre et al. 2017; Petrosino et al. 2021a). At CF caldera, the possible interaction of meteoric water and hydrothermal fluids contributes to the evolutions of the fluid movement and gas transfer (Chiodini et al. 2017; Petrosino et al. 2018) and, as a consequence, to the modulation of the seismicity. Indeed, the comparison between rainfall and raw seismicity time series suggests a close relationship during both SRI and HRI (Fig. 5). The seismicity distribution well matches the pore pressure change related to the rainfall amount (Fig. 5b and c). This is particularly evident during the HRI when most part of earthquakes occur in time intervals characterized by high changes in pore pressure (Fig. 5c). Likely, during the wet season, the effect of rainfall infiltration and pore pressure changes is dominant compared to both endogenous sources and exogenous processes of other nature.

Although we observe a delay in the correlation related to the percolation towards the fluid reservoir, the correlations are significant for both raw and declustered seismicity catalogues during the SRI (Fig. 6a and b). From the observed delay, we can expect that the rainwater infiltration into the low-permeability caprock and alteration of pore pressure takes from months to weeks in the case of low-permeability rocks which is also evident in the lag correlation between rainfall and associated pore pressure change (Hainzl et al. 2006; Wang et al. 2012; Petrosino et al. 2021a) (Figure S16). The seasonal induction of the pore pressure change over a long period generates enough force to impact the endogenous processes of deformation due to volatile expansions. On the contrary, as suggested from the behaviour of the seismicity, during the HRI, the endogenous processes are much more dominant and can be modulated by the combination of seasonal rainfall and tidal loadings producing short-period periodicity as better explained in the next section.

Tidal loading-induced modulation and deformation mechanism

Diurnal, fortnightly and monthly tidal periodicities in ground deformation and seismicity have been observed at CF caldera (Petrosino et al. 2018; Falanga et al. 2019). Specifically, Petrosino et al. (2018) found semi-diurnal periodicities in the earthquake rate that occurred from 2005 to 2016; however, they did not distinguish between tidal modulation effects in the low and high rate of inflation because they did not separate the investigated time interval. In our work, we have taken a step forward because we observe the semi-diurnal periodicity only in the declustered catalogue during the HRI. This provides strong evidence that short-period tidal triggering dominates in the HRI (Fig. 7). Further, the tidal stress correlation in the bar chart and N_{ex} values suggests

the occurrence of events during extensional horizontal NS stress (Fig. 8). This gives an idea about the mechanism that the extensional horizontal stress creates fractional openings in the pore spaces, which helps in the movement of hydrothermal exsolved fluids (De Lauro et al. 2013; Falanga et al. 2019).

The exothermic expansion of volatiles in the low permeability cap rocks of the aquifer widens the openings and creates interstitial pathways for the volatile-rich fluids (Lima et al. 2009; Chiodini et al. 2021). This phenomenon is only possible when the hydrothermal fluids are highly confined by the low permeability cap rocks and experience an expansion of the exsolved gaseous volatiles. We suggest that during the HRI, the amount of exsolution of volatiles is high, and exothermic expansion of the exsolved volatiles progressively achieves the gaseous or supercritical phase of the volatiles. Now, the movement of the volatile-rich fluid is significantly restricted by the low permeability cap rocks, which highly inflate the shallow hydrothermal reservoir and contribute to the increase in the rate of inflation of the reservoir and surface displacements. The isobaric expansion of the reservoir generates decompression of the pore spaces for the movement of the volatile-rich fluids. The tidal decompressions contribute to the expansions of pre-existing pore spaces and openings. This leads to a fractional opening in the cap rock, generation of the movement of the fluid into fractures, and squeezing out of the low-permeability rocks. The fluids circulating through the openings reach the end of the low permeability cap rock, impart maximum pressure on the wall due to expansions, and depart by generating brittle deformations in the rock. The fluids then precipitate in the openings, again sealing them, and the inflation gradually increases. This is also synchronous to the time intervals when enhanced gas emissions occur (Chiodini et al. 2015), as well as with the occurrence of seismicity due to brittle deformations accompanying the gradual inflation of the system. According to our results, the combined effect of rainfall, pore pressure increment, and tidal forcing increases the load at the aquifer due to water infiltration and induces instability of the reservoir host rock. This provides high magnitudes of confining stress to the hydrothermal reservoir, which is already constricted by the aquifer cap rock (Fig. 10). Thus, during the opening phase driven by extensional NS horizontal tidal stress, the hydrothermal fluids circulate through the openings and reach the permeable zone. This mechanism can trigger part of the seismicity, as already shown by Petrosino et al. (2018), Falanga et al. (2019), and Ricco et al. (2019). Although the effects of the Earth's tide have been previously reported in those works, the tidal modulations that we observed only in the HRI highlight the processes involved in the highly inflated and critically stressed system. We have tried to explain these processes through the fault resonance phenomenon.

Modelling the mechanism of exogenous modulation in the CF unrest context

Rainfall and tidal loadings are the most common and effective long-period (seasonal/annual) and short-period (diurnal/semi-diurnal) natural forces, respectively, that exert substantial loading/unloading on the Earth's surface. The CF caldera experiences moderate amounts of rainfall (~ 120 mm per month during wet seasons) and appreciable tidal loading (~ 1 to 1.2 kPa) as exogenous stress (Petrosino et al. 2018). In this context, our results provide evidence that, besides endogenous processes, exogenous sources also contribute to modulating ground deformation in the reservoir rocks and the associated seismicity. On the basis of the results, we have proposed a fault resonance model able to explain the complex multiple driving mechanisms undergoing in the CF caldera system, whose different responses appear to be dependent on the rate of inflation. A schematic representation of the outcomes of this model is shown in Fig. 10. The complex association of the seismicity and rainfall and its variation throughout the year can be referred to as a failure mechanism, modulated by the seasonality, and enhanced by the crustal structure of the region. Indeed, the CF caldera hosts shallow aquifers (Solfatara, Pisciarelli), thermal water springs (Agnano basin), and crater lakes (Astroni, Avernus) whose water flow rate is increased by the meteoric input. Moreover, seawater infiltration from the bay of Pozzuoli is favoured by the seasonal change in mean sea level associated with the reduction in atmospheric pressure, which usually occurs during rainfall periods (Palumbo and Mazzarella 1982; Scafetta and Mazzarella 2021; Dumont et al. 2022b). All these exogenous processes contribute to the increase of the hydrostatic load and pore pressure build-up (Palumbo and Mazzarella 1982; Petrosino et al. 2018), which is maximum during the wet seasons. The interaction of meteoric water with magmatic fluids and the increase in pore pressure contribute to the instability of the soil and low-permeability reservoir rocks, accelerating the deformation and the associated seismicity. This would explain the observed good correlation between the seismicity and rainfall amount (Figs. 4 and 6).

The pore pressure change due to rainfall and the dominant endogenous processes related to magmatic and hydrothermal fluid migration provide sufficient pre-requisite stress conditions to force the reservoir into a critical state. In this condition, although the tidal loading amplitudes are not very high (1–1.2 kPa) at the CF caldera, the reservoir becomes prone to tidal triggering (Petrosino et al. 2018; Sahoo et al. 2021), which does not require any threshold of loading amplitude (Ziv and Rubin 2000). This is also supported by fault resonance modelling analysis which suggests that a high inflation rate (as during the HRI) can make the magmatic system sensitive to tidal deformation. The existence of such tidal

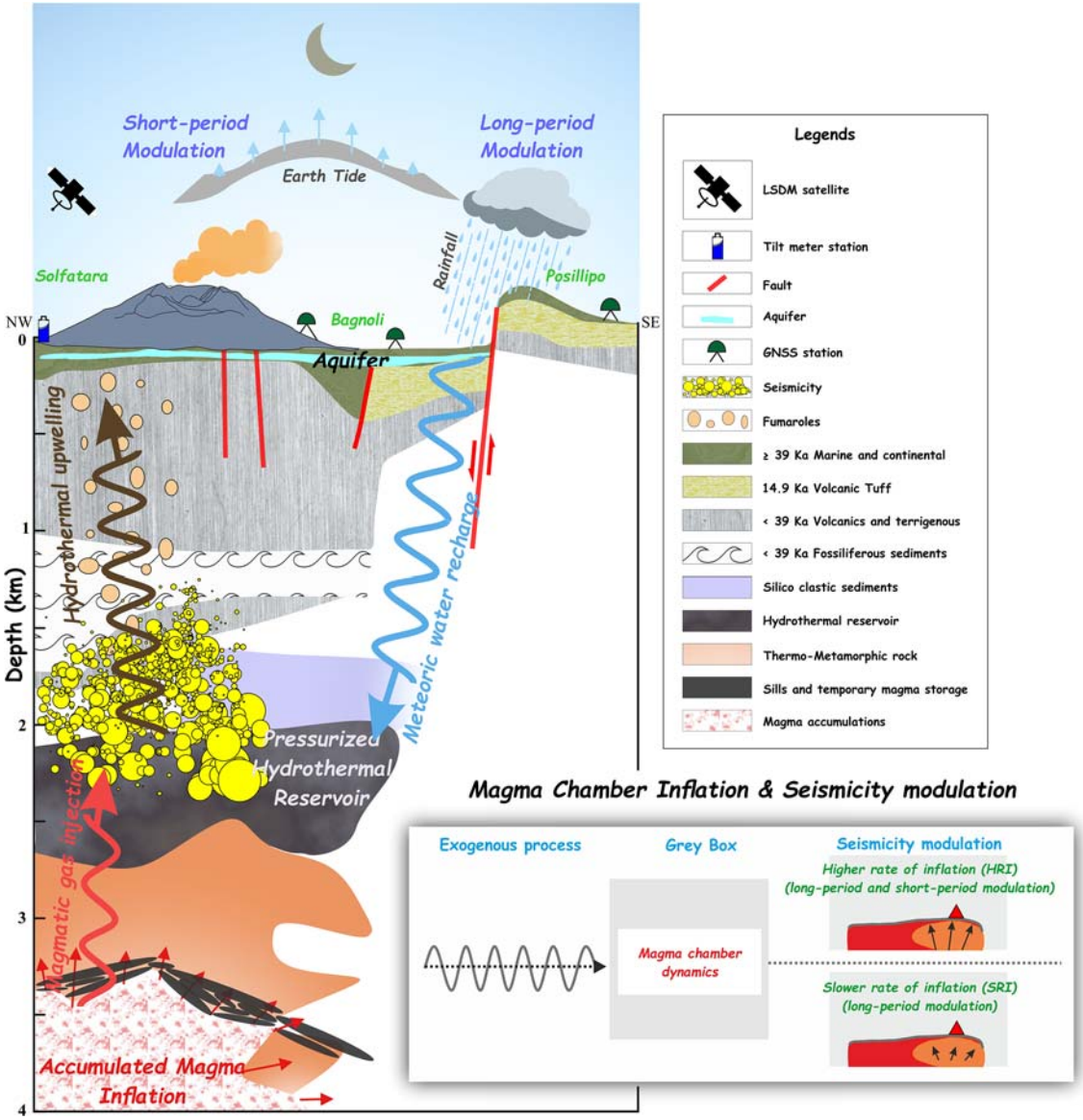

Fig. 10 Schematic representation of different exogenous processes (short-period tidal stress and long-period seasonal load) acting on the Campi Flegrei caldera and associated lithology, different features such as fault planes with a cross-sectional view. Inset shows the representation of possible mechanisms of short- and long-period exogenous processes for seismicity modulation during the SRI and HRI. During the HRI, the higher inflation rate due to higher displacements can generate both long- and short-period modulations, whereas in the case of the SRI, the lower displacements and lower inflation rate can only generate long-period modulations

effects on the CF reservoir dynamics at the CF caldera has been already ascertained by the ground tilt analyses (Falanga et al. 2019). The tidal correlation on a semi-diurnal time scale that we observed in the declustered seismicity suggests that although the swarms or clusters of earthquakes are mostly due to rainfall-induced pore pressure variations and pre-existing endogenous processes resulting in ground deformation, the declustered or primary events are triggered by tidal loading on the CF caldera.

At CF caldera, past studies have already provided evidence of the combined forcing of rainfall and tides on the endogenous processes (Chiodini et al. 2021; Falanga et al. 2019; Petrosino et al. 2018), yet, such experimental observations have not been interpreted in the frame of a physical model which could account for the mechanisms of the interactions. Our proposed model based on fault resonance destabilization explains the disparity in the behaviour of the seismicity in response to the different exogenous sources of stress perturbations during the SRI and HRI. In fact, according to the model, the SRI is only capable of destabilizing the volcanic system at the long period (annual, related to rainfall cycle) periodicity,

whereas the HRI can resonate destabilization in both long (long-period, annual) and short (short-period, semi-diurnal, related to tidal cycle) periodicity (Figs. 9 and 10).

Conclusions

The results of the present study, corroborated by robust statistical analyses, provide new insights into the variable degree of inflation (SRI and HRI) of the CF magmatic system and the associated seismicity modulation due to exogenous process-induced feedback mechanisms. The current study suggests that the seismicity occurs at the shallow and gas-rich fractured impermeable rock layer, where, the fluid exsolution from the magma crystallization and volumetric expansion of volatiles generate brittle deformations along the fracture zones before outgassing. From the modelling results, the source of surface deformation was found to be due to the inflation of shallow hydrothermal reservoirs. However, we understand that discrimination between a pressurization due to magmatic injections of fluid or an increase of pressure due to degassing from the mixing of hydrothermal fluids required additional constraints from other geological, geophysical, and geochemical observations. During the expansion and deformation, the fracture propagation due to outgassing and the sealing of fractures by crystallization and deposition continue in a cyclic manner. This makes the reservoir critically stressed and therefore more sensitive to exogenous processes. The external sources (acting on both long- and short-period) do not affect the general trend of inflation and rate of the uplift but are effective in generating cyclic fracturing and sealing of the hydrothermal system, thus modulating the seismicity simultaneously. Additionally, long-period seasonal modulations are observed during both the SRI and HRI, whereas short-period (semi-diurnal tidal) modulations are only detected during the HRI. We suggest that the tidal horizontal NS decompressions provide an additional extension to the volatile gas expansions and contribute to fracture propagation in the weakly permeable layer. For the first time, we proposed a physical model, the resonance destabilization model, which is able to explain the effects of the external forcing on the magmatic system and supports the hypothesis of sensitivity to different periodic perturbations during the evolution of the degree of inflation of the system. This observation of variation in modulation due to exogenous processes and associated deformation mechanisms during the degree of inflation of the magma chamber is unique and also represents a complex interplay between exogenous and endogenous processes on the CF caldera dynamics and hydrothermal system.

Datasets and codes availability statement

The topographic map presented in Fig. 1 has been generated using the Global Multi-Resolution Topography (GMRT) by rectangular area search with GeoTIFF output (https://www.gmrt.org/GMRTMapTool/). The tidal stress is computed using the SPOTL (Some Programs for Ocean-Tide Loading), SIO Technical Report, and Scripps Institution of Oceanography (Agnew 2012) (version 3.3.0.2; https://igppweb.ucsd.edu/~agnew/Spotl/spotlmain.html). The figures are generated by Grapher graphical application (version 8.7.844 https://www.goldensoftware.com/products/grapher), Surfer graphical application (version 8.7.844 URL: https://www.goldensoftware.com/products/surfer), Generic Mapping Tools (Wessel et al. 2019) (version 5.2.1; https://www.generic-mapping-tools.org/), Python Matplotlib package (https://www.python.org/), and Corel Draw graphical application (version 18; https://www.coreldraw.com/en). The seismicity catalogue compiled by INGV-OV for Campi Flegrei is publicly available on the domain (http://sismolab.ov.ingv.it/sismo/index.php?PAGE=SISMO/last&area=Flegrei). The GNSS displacement dataset from 2005 to 2019 was taken from De Martino et al. (2021) which is publicly archived at the supplementary information (https://doi.org/10.3390/rs13142725). The rainfall and atmospheric data were downloaded from the public archives of the Italian authority (https://www.wunderground.com/weather/it/positano/LIRN/date/20194, https://www.3bmeteo.com/meteo/ora/storico/202201). The rainfall data are also collected from satellite-derived rainfall observations from GPM (ftp://arthurhou.pps.eosdis.nasa.gov/gpmdata/) for the pore-pressure modelling. We have used the publicly archived ground temperature data from the SF1 infrared thermal camera (Cusano et al. 2021b) (https://zenodo.org/record/5109809#.YdQqN2jMJPY) and the publicly archived root mean square (RMS) ground tilt data from the CMP tiltmeter (Petrosino et al. 2021b) (https://zenodo.org/record/5196688#.YdQqP2jMJPY). The Hydrological Land Surface Discharge Model (LSDM), data, and programs are provided by the German Research Center for Geosciences (GFZ) (http://rz-vm115.gfz-potsdam.de:8080/repository). All relevant codes are available from the authors upon reasonable request.

Supplementary Information The online version contains supplementary material available at https://doi.org/10.1007/s00445-024-01719-7.

Acknowledgements This work has been performed within the framework of Sambit Sahoo's PhD thesis at NIT Rourkela under the supervision of Dr. Bhaskar Kundu. We acknowledge Batakrushna Senapati from the Tectonic Geodesy Lab (https://www.tectonicgeodesylab.in/) for his help in fault resonance modelling. We would also like to thank Dr. Nico Fournier, Editor, and the two anonymous reviewers for their constructive comments and suggestions, which significantly improved the quality of the work.

Author contribution B. K. and S.P. provided research ideas. S.S. performed all the analysis. D.T. performed the pore-pressure modelling from the GPM dataset. B. K. and R.K.Y. performed the GNSS inversion modelling. S.S. and S.P. wrote the original draft. B. K., S.P., and S.J. reviewed and edited the draft and interpreted the results. All authors contributed equally and took part in finalizing the manuscript.

Funding SS is supported by the CSIR-UGC fellowship. DT is financially supported by the Ministry of Earth Sciences, Government of India, through grant no. MoES/P.O.(Seismo)/1(349)/2018. R.K.Y. is thankful to National Geophysical Research Institute, Hyderabad, India for the support. This is NGRI publication number NGRI/Lib/2024/Pub-26. This work is financially supported by the National Natural Science Foundation of China (NSFC) Project (grant no. 12073012).

National Natural Science Foundation of China-Henan Joint Fund,12073012,Shuanggen Jin

Declarations

Competing interests The authors declare no competing interests.

References

Ader TJ, Avouac JP (2013) Detecting periodicities and declustering in earthquake catalogs using the Schuster spectrum, application to Himalayan seismicity. Earth Planet Sci Lett 377:97–105. https://doi.org/10.1016/j.epsl.2013.06.032

Agnew DC (1997) NLOADF: a program for computing ocean-tide loading. J Geophys Res Solid Earth 102(B3):5109–5110. https://doi.org/10.1029/96JB03458

Agnew, D. C. (1996). SPOTL: some programs for ocean-tide loading. SIO Ref. Ser. 96–8. Scripps Instit of Oceanogr, La Jolla, Calif, 35. https://doi.org/10.1029/96JB03458

Agnew, D. C. (2012). SPOTL: some programs for ocean-tide loading. https://escholarship.org/uc/item/954322pg

Amoruso A, Crescentini L, Berrino G (2008) Simultaneous inversion of deformation and gravity changes in a horizontally layered half-space: Evidences for magma intrusion during the 1982–1984 unrest at Campi Flegrei caldera (Italy). Earth Planet Sci Lett 272(1–2):181–188. https://doi.org/10.1016/j.epsl.2008.04.040

Amoruso A, Crescentini L (2022) Clues of ongoing deep magma inflation at Campi Flegrei caldera (Italy) from empirical orthogonal function analysis of SAR data. Remote Sens 14(22):5698

Amoruso A, Crescentini L, Sabbetta I (2014a) Paired deformation sources of the Campi Flegrei caldera (Italy) required by recent (1980–2010) deformation history. J Geophys Res Solid Earth 119(2):858–879. https://doi.org/10.1002/2013JB010392

Amoruso A, Crescentini L, Sabbetta I, De Martino P, Obrizzo F, Tammaro U (2014b) Clues to the cause of the 2011–2013 Campi Flegrei caldera unrest, Italy, from continuous GNSS data. Geophys Res Lett 41(9):3081–3088. https://doi.org/10.1002/2014GL059539

Barton G, Barton G (1989) Elements of Green's functions and propagation: potentials, diffusion, and waves. Oxford University Press

Battaglia J, Zollo A, Virieux J, Iacono DD (2008) Merging active and passive data sets in traveltime tomography: the case study of Campi Flegrei caldera (Southern Italy). Geophys Prospect 56(4):555–573. https://doi.org/10.1111/j.1365-2478.2007.00687.x

Battaglia M, Cervelli PF, Murray JR (2013) dMODELS: a MATLAB software package for modeling crustal deformation near active faults and volcanic centers. J Volcanol Geoth Res 254:1–4. https://doi.org/10.1016/j.jvolgeores.2012.12.018

Bellucci Sessa E, Castellano M, Ricciolino P (2021) GIS applications in volcano monitoring: the study of seismic swarms at the Campi Flegrei volcanic complex, Italy. Adv Geosci 52:131–144

Bevilacqua A, Isaia R, Neri A, Vitale S, Aspinall WP, Bisson M, Rosi M (2015) Quantifying volcanic hazard at Campi Flegrei caldera (Italy) with uncertainty assessment: 1 Vent opening maps. J Geophys Res Solid Earth 120(4):2309–2329. https://doi.org/10.1002/2014JB011775

Bevilacqua A, Neri A, De Martino P, Isaia R, Novellino A, Tramparulo FDA, Vitale S (2020) Radial interpolation of GNSS and leveling data of ground deformation in a resurgent caldera: application to Campi Flegrei (Italy). J Geodesy 94(2):1–27. https://doi.org/10.1007/s00190-020-01355-x

Calò M, Tramelli A (2018) Anatomy of the Campi Flegrei caldera using enhanced seismic tomography models. Sci Rep 8(1):1–12. https://doi.org/10.1038/s41598-018-34456-x

Campi Felgrei caldera, monthly surveillance bulletin, August 2022. https://www.ov.ingv.it/index.php/monitoraggio-e-infrastrutture/bollettini-tutti/bollett-mensili-cf/anno-2022-2/1138-bollettino-mensile-campi-flegrei-2022-08/file

Capuano P, Russo G, Civetta L, Orsi G, D'Antonio M, Moretti R (2013) The active portion of the Campi Flegrei caldera structure imaged by 3-D inversion of gravity data. Geochem Geophys Geosyst 14(10):4681–4697. https://doi.org/10.1002/ggge.20276

Caputo T, Cusano P, Petrosino S, Sansivero F, Vilardo G (2020) Spectral analysis of ground thermal image temperatures: what we are learning at Solfatara volcano (Italy). Adv Geosci 52:55–65. https://doi.org/10.5194/adgeo-52-55-2020

Carlino S (2021) Brief history of volcanic risk in the Neapolitan area (Campania, southern Italy): a critical review. Nat Hazard 21(10):3097–3112. https://doi.org/10.5194/nhess-21-3097-2021

Chiodini G, Caliro S, De Martino P, Avino R, Gherardi F (2012) Early signals of new volcanic unrest at Campi Flegrei caldera? Insights from geochemical data and physical simulations. Geology 40(10):943–946. https://doi.org/10.1130/G33251.1

Chiodini G, Selva J, Del Pezzo E, Marsan D, De Siena L, D'auria L, Petrillo Z (2017) Clues on the origin of post-2000 earthquakes at Campi Flegrei caldera (Italy). Sci Rep 7(1):4472. https://doi.org/10.1038/s41598-017-04845-9

Chiodini G, Caliro S, Avino R, Bini G, Giudicepietro F, De Cesare W, Tripaldi S (2021) Hydrothermal pressure-temperature control on CO2 emissions and seismicity at Campi Flegrei (Italy). J Volcanol Geothermal Res 414:107245. https://doi.org/10.1016/j.jvolgeores.2021.107245

Chiodini G, Caliro S, Cardellini C, Granieri D, Avino R, Baldini A, Donnini M, Minopoli C (2010). Long-term variations of the Campi Flegrei, Italy, volcanic system as revealed by the monitoring of hydrothermal activity. J Geophys Res Solid Earth 115(B3). https://doi.org/10.1029/2008JB006258

Chiodini G, Vandemeulebrouck J, Caliro S, D'Auria L, De Martino P, Mangiacapra A, Petrillo Z (2015) Evidence of thermal-driven processes triggering the 2005–2014 unrest at Campi Flegrei caldera. Earth Planet Sci Lett 414:58–67. https://doi.org/10.1016/j.epsl.2015.01.012

Cochran ES, Vidale JE, Tanaka S (2004) Earth tides can trigger shallow thrust fault earthquakes. Science 306(5699):1164–1166. https://doi.org/10.1126/science.1103961

Cusano P, Caputo T, De Lauro E, Falanga M, Petrosino S, Sansivero F, Vilardo G (2021a) Tracking the internal dynamics of the Solfatara volcano (Campi Flegrei, Italy) through the analysis

of ground thermal image temperatures. Atmosphere 12(8):940. https://doi.org/10.3390/atmos12080940

Cusano P, Caputo T, De Lauro E, Falanga M, Petrosino S, Sansivero F, Vilardo G (2021b) Ground thermal image temperatures (Campi Flegrei and Vesuvius) and atmospheric temperature and pressure. Zenodo. https://doi.org/10.5281/zenodo.5109809

D'Auria L, Pepe S, Castaldo R, Giudicepietro F, Macedonio G, Ricciolino P, Zinno I (2015) Magma injection beneath the urban area of Naples: a new mechanism for the 2012–2013 volcanic unrest at Campi Flegrei caldera. Sci Rep 5(1):1–11. https://doi.org/10.1038/srep13100

D'Auria L, Giudicepietro F, Aquino I, Borriello G, Del Gaudio C, Lo Bascio D, Martini M, Ricciardi GP, Ricciolino P, Ricco C (2011) Repeated fluid-transfer episodes as a mechanism for the recent dynamics of Campi Flegrei caldera (1989–2010) J Geophys Res Solid Earth 116 (B4) https://doi.org/10.1029/2010JB007837

De Lauro E, De Martino S, Falanga M, Petrosino S (2013) Synchronization between tides and sustained oscillations of the hydrothermal system of Campi Flegrei (Italy). Geochem Geophys Geosyst 14(8):2628–2637. https://doi.org/10.1002/ggge.20149

De Lauro E, De Martino S, Falanga M, Petrosino S (2016) Fast wavefield decomposition of volcano-tectonic earthquakes into polarized P and S waves by independent component analysis. Tectonophysics 690:355–361. https://doi.org/10.1016/j.tecto.2016.10.005GR

De Martino P, Tammaro U, Obrizzo F (2014) GPS time series at Campi Flegrei caldera (2000–2013). Ann Geophys. https://doi.org/10.4401/ag-6431

De Martino P, Dolce M, Brandi G, Scarpato G, Tammaro U (2021) The ground deformation history of the Neapolitan volcanic area (Campi Flegrei Caldera, Somma-Vesuvius Volcano, and Ischia Island) from 20 years of continuous GNSS observations (2000–2019). Remote Sens 13(14):2725. https://doi.org/10.3390/rs13142725

De Natale G, Troise C, Pingue F (2001) A mechanical fluid-dynamical model for ground movements at Campi Flegrei caldera. J Geodyn 32(4–5):487–517. https://doi.org/10.1016/S0264-3707(01)00045-X

De Siena L, Del Pezzo E, Bianco F (2010) Seismic attenuation imaging of Campi Flegrei: evidence of gas reservoirs, hydrothermal basins, and feeding systems. J Geophys Res Solid Earth 115(B9):1. https://doi.org/10.1029/2009JB006938

de Vivo B, Belkin HE, Barbieri M, Chelini W, Lattanzi P, Lima A, Tolomeo L (1989) The Campi Flegrei (Italy) geothermal system: a fluid inclusion study of the Mofete and San Vito fields. J Volcanol Geoth Res 36(4):303–326. https://doi.org/10.1016/0377-0273(89)90076-0

Del Gaudio C, Aquino I, Ricciardi GP, Ricco C, Scandone R (2010) Unrest episodes at Campi Flegrei: a reconstruction of vertical ground movements during 1905–2009. J Volcanol Geoth Res 195(1):48–56. https://doi.org/10.1016/j.jvolgeores.2010.05.014

Di Vito M, Lirer L, Mastrolorenzo G, Rolandi G (1987) The 1538 Monte Nuovo eruption (Campi Flegrei, Italy). Bull Volcanol 49(4):608–615. https://doi.org/10.1007/BF01079966

Di Vito MA, Isaia R, Orsi G, Southon JD, De Vita S, d'Antonio M, Piochi M (1999) Volcanism and deformation since 12,000 years at the Campi Flegrei caldera (Italy). J Volcanol Geotherm Res 91(2–4):221–246. https://doi.org/10.1016/S0377-0273(99)00037-2

Dill R, Dobslaw H (2013) Numerical simulations of global-scale high-resolution hydrological crustal deformations. J Geophys Res Solid Earth 118(9):5008–5017. https://doi.org/10.1002/jgrb.50353

Dong S, Kelly KA (2003) Seasonal and interannual variations in geostrophic velocity in the Middle Atlantic Bight. J Geophys Res Oceans 108(C6). https://doi.org/10.1029/2002JC001357

Dumont S, Petrosino S, Pyle D, Feuillet N (2022) External forcing on volcanoes and volcanic processes: observations, analysis and implications. Front Earth Sci 10:999214

Dumont S, Petrosino S, Neves MC (2022b) On the link between global volcanic activity and global mean sea level. Front Earth Sci 10:845511

Egbert GD, Erofeeva SY (2002) Efficient inverse modeling of barotropic ocean tides. J Atmos Oceanic Technol 19:183–204. https://doi.org/10.1175/1520-0426(2002)019%3c0183:EIMOBO%3e2.0.CO;2

D Emter 1997 Tidal triggering of earthquakes and volcanic events. Tidal phenomena, 293-309. https://doi.org/10.1007/BFb0011468

Falanga M, De Lauro E, Petrosino S, De Martino S (2019) Interaction between seismicity and deformation on different time scales in volcanic areas: Campi Flegrei and Stromboli. Adv Geosci 52:1–8. https://doi.org/10.5194/adgeo-52-1-2019

Falanga M, Aquino I, De Lauro E, Petrosino S, Ricco C (2023) New insights on ground deformation at Campi Flegrei caldera inferred from kinematics and dynamics investigation of borehole tilt. Earth Space Sci 10(3):e2022EA002702. https://doi.org/10.1029/2022EA002702

Farquharson JI, Amelung F (2020) Extreme rainfall triggered the 2018 rift eruption at Kīlauea Volcano. Nature 580(7804):491–495. https://doi.org/10.1038/s41586-020-2172-5

Farrell WE (1972) Deformation of the Earth by surface loads. Rev Geophys 10(3):761–797. https://doi.org/10.1029/RG010i003p00761

Hainzl S, Kraft T, Wassermann J, Igel H, Schmedes E (2006) Evidence for rainfall-triggered earthquake activity. Geophys Res Lett 33(19):1. https://doi.org/10.1029/2006GL027642

Hamilton WL (1973) Tidal cycles of volcanic eruptions: fortnightly to 19 yearly periods. J Geophys Res 78(17):3363–3375. https://doi.org/10.1029/JB078i017p03363

Heap MJ, Baud P, Meredith PG, Vinciguerra S, Reuschlé T (2014) The permeability and elastic moduli of tuff from Campi Flegrei, Italy: implications for ground deformation modelling. Solid Earth 5(1):25–44. https://doi.org/10.5194/se-5-25-2014

Kilburn CR, De Natale G, Carlino S (2017) Progressive approach to eruption at Campi Flegrei caldera in southern Italy. Nat Commun 8(1):1–8. https://doi.org/10.1038/ncomms15312

Kiyoo Mogi (1958) Relations between the eruptions of various volcanoes and the deformations of the ground surfaces around them. Earthq Res Inst 36:99–134 (https://radar.community.uaf.edu/wp-content/uploads/sites/667/2017/04/Mogi1958.pdf)

Kümpel HJ, Lehmann K, Fabian M, Mentes G (2001) Point stability at shallow depths: experience from tilt measurements in the Lower Rhine Embayment, Germany, and implications for high-resolution GNSS and gravity recordings. Geophys J Int 146(3):699–713. https://doi.org/10.1046/j.1365-246X.2001.00494.x

Lesparre N, Boudin F, Champollion C, Chery J, Danquigny C, Seat HC, Longuevergne L (2017) New insights on fractures deformation from tiltmeter data measured inside the Fontaine de Vaucluse karst system. Geophys J Int 208(3):1389–1402. https://doi.org/10.1093/gji/ggw446

Lima A, De Vivo B, Spera FJ, Bodnar RJ, Milia A, Nunziata C, Cannatelli C (2009) Thermodynamic model for uplift and deflation episodes (bradyseism) associated with magmatic–hydrothermal activity at the Campi Flegrei (Italy). Earth Sci Rev 97(1–4):44–58. https://doi.org/10.1016/j.earscirev.2009.10.001

Lima A, Bodnar RJ, De Vivo B, Spera FJ, Belkin HE (2021) Interpretation of recent unrest events (Bradyseism) at Campi Flegrei, Napoli (Italy): comparison of models based on cyclical

hydrothermal events versus shallow magmatic intrusive events. Geofluids 2021. https://doi.org/10.1155/2021/2000255
Lockner DA, Beeler NM (1999) Premonitory slip and tidal triggering of earthquakes. J Geophys Res Solid Earth 104(B9):20133–20151. https://doi.org/10.1029/1999JB900205
Manconi A, Walter TR, Manzo M, Zeni G, Tizzani P, Sansosti E, Lanari R (2010) On the effects of 3-D mechanical heterogeneities at Campi Flegrei caldera, southern Italy. J Geophys Res Solid Earth 115(B8):1. https://doi.org/10.1029/2009JB007099
Marone C (1998) Laboratory-derived friction laws and their application to seismic faulting. Annu Rev Earth Planet Sci 26:643–696. https://doi.org/10.1146/annurev.earth.26.1.643
Mason Ben G, Pyle David M, Brian Dade W, Jupp T (2004) Seasonality of volcanic eruptions. J Geophys Res Solid Earth 109(B4):1. https://doi.org/10.1029/2002JB002293
Mastrolorenzo G, Pappalardo L, Troise C, Rossano S, Panizza A, De Natale G (2006) Volcanic hazard assessment at the Campi Flegrei caldera. Geol Soc Spec Publ 269(1):159–171. https://doi.org/10.1144/GSL.SP.2006.269.01.10
McNutt SR, Beavan RJ (1987) Eruptions of Pavlof volcano and their possible modulation by ocean load and tectonic stresses. J Geophys Res Solid Earth 92(B11):11509–11523. https://doi.org/10.1029/JB092iB11p11509
McTigue DF (1987) Elastic stress and deformation near a finite spherical magma body: resolution of the point source paradox. J Geophys Res Solid Earth 92(B12):12931–12940. https://doi.org/10.1029/JB092iB12p12931
Métivier L, de Viron O, Conrad CP, Renault S, Diament M, Patau G (2009) Evidence of earthquake triggering by the solid earth tides. Earth Planet Sci Lett 278(3–4):370–375. https://doi.org/10.1016/j.epsl.2008.12.024
Moretti R, Troise C, Sarno F, De Natale G (2018) Caldera unrest driven by CO2-induced drying of the deep hydrothermal system. Sci Rep 8(1):1–11. https://doi.org/10.1038/s41598-018-26610-2
Nespoli M, Belardinelli ME, Bonafede M (2021) Stress and deformation induced in layered media by cylindrical thermo-poro-elastic sources: an application to Campi Flegrei (Italy). J Volcanol Geoth Res 415:107269. https://doi.org/10.1016/j.jvolgeores.2021.107269
Newhall CG, & Dzurisin D (1988) Historical unrest at the large calderas of the world (No. 1855). Department of the Interior US Geological Survey. https://doi.org/10.3133/b1855
Niu J, Song TRA (2021) The response of repetitive very-long-period seismic signals at Aso Volcano to periodic loading. Geophys Res Lett 48(9):e2021GL092728. https://doi.org/10.1029/2021GL092728
Orsi G, De Vita S, Di Vito M (1996) The restless, resurgent Campi Flegrei nested caldera (Italy): constraints on its evolution and configuration. J Volcanol Geoth Res 74(3–4):179–214. https://doi.org/10.1016/S0377-0273(96)00063-7
Orsi G, Di Vito MA, Isaia R (2004) Volcanic hazard assessment at the restless Campi Flegrei caldera. Bull Volcanol 66(6):514–530. https://doi.org/10.1007/s00445-003-0336-4
Palumbo A, Mazzarella A (1982) Mean sea level variations and their practical applications. J Geophys Res Oceans 87(C6):4249–4256. https://doi.org/10.1029/JC087iC06p04249
Parascandola, A. (1947). I fenomeni bradisismici del Serapeo di Pozzuoli. Stabilmento tipografico G. Genovese
Perfettini H, Schmittbuhl J, Rice JR, Cocco M (2001) Frictional response induced by time-dependent fluctuations of the normal loading. J Geophys Res Solid Earth 106(B7):13455–13472. https://doi.org/10.1029/2000JB900366
Petrosino S, De Siena L (2021) Fluid migrations and volcanic earthquakes from depolarized ambient noise. Nat Commun 12(1):6656. https://doi.org/10.1038/s41467-021-26954-w
Petrosino S, Dumont S (2022) Tidal modulation of hydrothermal tremor: examples from Ischia and Campi Flegrei volcanoes Italy. Front Earth Sci 9:775269. https://doi.org/10.3389/feart.2021.775269
Petrosino S, Cusano P, Madonia P (2018) Tidal and hydrological periodicities of seismicity reveal new risk scenarios at Campi Flegrei caldera. Sci Rep 8(1):1–12. https://doi.org/10.1038/s41598-018-31760-4
Petrosino S, Ricco C, Aquino I (2021a) Modulation of ground deformation and earthquakes by rainfall at Vesuvius and Campi Flegrei (Italy). Front Earth Sci. https://doi.org/10.3389/feart.2021.758602
Petrosino S., Ricco C., & Ida Aquino. (2021b). Dailly root mean square (RMS) of tiltmeter data recorded at Vesuvius and Campi Flegrei [data set] Zenodo 10.5281/zenodo.5196688
Phillipson G, Sobradelo R, Gottsmann J (2013) Global volcanic unrest in the 21st century: an analysis of the first decade. J Volcanol Geoth Res 264:183–196. https://doi.org/10.1016/j.jvolgeores.2013.08.004
Pollitz FF, Wech A, Kao H, Bürgmann R (2013) Annual modulation of non-volcanic tremor in northern Cascadia. J Geophys Res Solid Earth 118(5):2445–2459. https://doi.org/10.1002/jgrb.50181
Ray, R.D. (1999). A global ocean tide model from TOPEX/POSEIDON altimetry: GOT99. 2. National Aeronautics and Space Administration, Goddard Space Flight Center.
Ricco C, Petrosino S, Aquino I, Del Gaudio C, Falanga M (2019) Some investigations on a possible relationship between ground deformation and seismic activity at Campi Flegrei and Ischia volcanic areas (Southern Italy). Geosciences 9(5):222. https://doi.org/10.3390/geosciences9050222
Rudnicki JW (1986) Fluid mass sources and point forces in linear elastic diffusive solids. Mech Mater 5(4):383–393. https://doi.org/10.1016/0167-6636(86)90042-6
Rydelek PA, Davis PM, Koyanagi RY (1988) Tidal triggering of earthquake swarms at Kilauea volcano Hawaii. J Geophys Res Solid Earth 93(B5):4401–4411. https://doi.org/10.1029/JB093iB05p04401
Saccorotti G, Petrosino S, Bianco F, Castellano M, Galluzzo D, La Rocca M, Cusano P (2007) Seismicity associated with the 2004–2006 renewed ground uplift at Campi Flegrei Caldera, Italy. Phys Earth Planet Inter 165(1–2):14–24
Sahoo S, Senapati B, Panda D, Tiwari DK, Santosh M, Kundu B (2021) Tidal triggering of micro-seismicity associated with caldera dynamics in the Juan de Fuca ridge. J Volcanol Geoth Res 417:107319. https://doi.org/10.1016/j.jvolgeores.2021.107319
Sahoo S, Tiwari DK, Panda D, Kundu B (2022) Eruption cycles of Mount Etna triggered by seasonal climatic rainfall. J Geodyn 149:101896. https://doi.org/10.1016/j.jog.2021.101896
Sansivero F., Vilardo G. (2022). Ground-based thermal/IR images acquired by TIRNet permanent volcanic surveillance network. Istituto Nazionale di Geofisica e Vulcanologia (INGV) https://doi.org/10.13127/vd/tirnet
Scafetta N, Mazzarella A (2021) On the rainfall triggering of Phlegraean Fields volcanic tremors. Water 13(2):154. https://doi.org/10.3390/w13020154
Scholz CH (1998) Earthquakes and friction laws. Nature 391(6662):37–42. https://doi.org/10.1038/34097
Senapati B, Kundu B, Jin S (2022) Seismicity modulation by external stress perturbations in plate boundary vs. stable plate interior. Geosci Front 13(3):101352. https://doi.org/10.1016/j.gsf.2022.101352
Senapati B, Kundu B, Perfettini H, Gahalaut VK, Singh AK, Ghosh A, Rao NP (2023) Fault resonance process and its implications on

seismicity modulation on the active fault system. Tectonophysics 861:229920. https://doi.org/10.1016/j.tecto.2023.229920

Tan YJ, Tolstoy M, Waldhauser F, Bohnenstiehl DR (2018) Tidal triggering of microearthquakes over an eruption cycle at 9 50′N East Pacific Rise. Geophys Res Lett 45(4):1825–1831. https://doi.org/10.1002/2017GL076497

Tanaka S, Sato H, Matsumura S, Ohtake M (2006) Tidal triggering of earthquakes in the subducting Philippine Sea plate beneath the locked zone of the plate interface in the Tokai region Japan. Tectonophysics 417(1–2):69–80. https://doi.org/10.1016/j.tecto.2005.09.013

Tedesco D (1994) Chemical and isotopic gas emissions at Campi Flegrei: evidence for an aborted period of unrest. J Geophys Res Solid Earth 99(B8):15623–15631. https://doi.org/10.1029/94JB00465

Thomas AM, Bürgmann R, Shelly DR et al (2012) Tidal triggering of low frequency earthquakes near Parkfield, California: implications for fault mechanics within the brittle-ductile transition. J Geophys Res 117. https://doi.org/10.1029/2011JB009036

Trasatti E, Polcari M, Bonafede M, Stramondo S (2015) Geodetic constraints to the source mechanism of the 2011–2013 unrest at Campi Flegrei (Italy) caldera. Geophys Res Lett 42(10):3847–3854. https://doi.org/10.1002/2015GL063621

Troise C, De Natale G, Schiavone R, Somma R, Moretti R (2019) The Campi Flegrei caldera unrest: discriminating magma intrusions from hydrothermal effects and implications for possible evolution. Earth Sci Rev 188:108–122. https://doi.org/10.1016/j.earscirev.2018.11.007

Vilardo G, Chiodini G, Augusti V, Granieri D, Caliro S, Minopoli C, & Terranova C (2008). The permanent thermal infrared network for the monitoring of hydrothermal activity at the Solfatara and Vesuvius volcanoes. In Conception, verification and application of innovative techniques to study active volcanoes. Istituto Nazionale di Geofisica e Vulcanologia

Wang H, Xiang L, Jia L, Jiang L, Wang Z, Hu B, Gao P (2012) Load Love numbers and Green's functions for elastic earth models PREM, iasp91, ak135, and modified models with refined crustal structure from Crust 2.0. Comput Geosci 49:190–199. https://doi.org/10.1016/j.cageo.2012.06.022

Wessel P, Luis JF, Uieda L, Scharroo R, Wobbe F, Smith WH, Tian D (2019) The generic mapping tools version 6. Geochem Geophys Geosyst 20(11):5556–5564. https://doi.org/10.1029/2019GC008515

Wilcock WSD, Tolstoy M, Waldhauser F, Garcia C, Tan YJ, Bohnenstiehl DR, Caplan-Auerbach J, Dziak RP, Arnulf AF, Everett Mann M (2016) Seismic constraints on caldera dynamics from the 2015 Axial Seamount eruption Volcano monitoring goes into the deep. Science 354(6318):1395–1399. https://doi.org/10.1126/science.aah5563

Ziv A, Rubin AM (2000) Static stress transfer and earthquake triggering: no lower threshold in sight? J Geophys Res 105:13631–13642. https://doi.org/10.1029/2000JB900081

Zollo A, Maercklin N, Vassallo M, Dello Iacono D, Virieux J, Gasparini P (2008) Seismic reflections reveal a massive melt layer feeding Campi Flegrei caldera. Geophys Res Lett 35(12). https://doi.org/10.1029/2008GL034242